IEEE Access
Multidisciplinary | Rapid Review | Open Access Journal

Received 10 September 2023, accepted 24 September 2023, date of publication 4 October 2023, date of current version 13 October 2023.

Digital Object Identifier 10.1109/ACCESS.2023.3321859

RESEARCH ARTICLE

Novel Design of Lightweight Aerial Manipulator for Solar Panel Cleaning Applications

MUHANNAD ALKADDOUR[1], (Member, IEEE), MOHAMMAD A. JARADAT[1], SARA TELLAB[2], NIDAL A. SHERIF[2], MUHAMMAD H. ALVI[1], LOTFI ROMDHANE[1], (Member, IEEE), AND KHALED S. HATAMLEH[3]

[1]Department of Mechanical Engineering, American University of Sharjah, Sharjah, United Arab Emirates
[2]Mechatronics Engineering Graduate Program, American University of Sharjah, Sharjah, United Arab Emirates
[3]Mechanical Engineering Department, Jordan University of Science and Technology, Irbid 22110, Jordan

Corresponding author: Mohammad A. Jaradat (mjaradat@aus.edu)

This work was supported in part by the American University of Sharjah (AUS), Faculty Research Grant (FRG) Program under Grant EFRG18-SCR-CEN-34; and in part by the Open Access Program from the American University of Sharjah.

ABSTRACT In this research, a novel design of a lightweight aerial manipulator system is proposed for solar panel cleaning with active (CoG) compensation mechanism. Recently, separate solar panel arrays or units are commonly installed on residential, commercial rooftops or roads, making it inconvenient for land robots to perform the cleaning tasks. The proposed light weight solar panel cleaning aerial manipulator with the gravity compensation mechanism is intended to be attached beneath a drone to increase its stability during operation. The manipulator workspace given the proposed system is analyzed under CoG shift constraints. The kinematics and dynamics of the aerial manipulator coupled with the compensation mechanism are presented, and a path-planning scheme for solar panel cleaning is detailed. A dynamic control law based on pitch and counterweight position reduced-order dynamics is derived, and its equivalence to the static compensation law is shown. An experimental test bench is used to simulate the aerial manipulation during operations to validate the performance of the proposed manipulator and its stability. Its tilting pitch angle is collected and examined during operation. The results show that the system is less susceptible to unwanted tilting. A tilt angle reduction of 2 degrees was observed between an uncompensated and compensated system, with a difference in shift of CoG location of 1.72% of the total system length. The CoG location shift is also simulated without the presence of a slider mechanism and shows a difference of 24.5% with the compensated system. The compensation mechanism significantly reduces the tilt angle, avoiding potential instability, and consequently decreases the power required by the carrying drone.

INDEX TERMS Solar panel cleaning aerial manipulator, aerial manipulators, CoG compensation mechanism.

NOMENCLATURE

$c_i,\ s_i$	$\cos q_i, \sin q_i$.
$c_{q_xq_y},\ s_{q_xq_y}$	$\cos\left(q_x - q_y\right), \sin\left(q_x - q_y\right)$.
$\mathbb{R}^n,\ \mathbb{R}^{m\times n}$	The spaces of $n-$vectors and $m\times n$ matrices with real entries.
$\boldsymbol{e}_i$	i^{th} element of the standard basis of $\mathbb{R}^n$.
$A^T,\ A^{-1}$	Transpose and matrix inverse.
$\frac{\partial a}{\partial \boldsymbol{x}}$	Gradient with $a \in\mathbb{R}$, $\boldsymbol{x}\in\mathbb{R}^n$, $\frac{\partial a}{\partial \boldsymbol{x}}\in\mathbb{R}^n$.
$\frac{\partial A}{\partial x}$	Derivative with $A\in\mathbb{R}^{m\times n}$, $x\in\mathbb{R}$, $\frac{\partial A}{\partial x}\in\mathbb{R}^{m\times n}$.
$\frac{\partial \boldsymbol{a}}{\partial \boldsymbol{x}}$	Jacobian with $\boldsymbol{a}\in\mathbb{R}^m$, $\boldsymbol{x}\in\mathbb{R}^n$, $\frac{\partial \boldsymbol{a}}{\partial \boldsymbol{x}}\in\mathbb{R}^{m\times n}$.
$\dot{\boldsymbol{x}}\ddot{\boldsymbol{x}}$	Time derivatives of $\boldsymbol{x}$.
$\|\cdot\|$	Euclidean norm .
$\boldsymbol{I}_n,\ \boldsymbol{0}_n$	Identity and square zero matrices of size n.
$\boldsymbol{0}_{m\times n}$	Zero matrix with dimension $m\times n$.
$E_{a_1,\ \ldots,\ a_n}$	Selection matrix to choose matrix elements in positions specified a_1 through a_n.
t	Time.
g	Gravitational acceleration ($=9.81\frac{m}{s^2}$).
$\boldsymbol{g}$	Vector of magnitude g in the direction of gravity.

The associate editor coordinating the review of this manuscript and approving it for publication was Guilin Yang.

$\mathcal{F}_E, \mathcal{F}_M, \mathcal{F}_B, \mathcal{F}_S$	Earth, manipulator, hexacopter, and solar panel frames.
$\mathcal{F}_i, \mathcal{F}_n$	Link i and end-effector frames.
$\boldsymbol{p}_x^y$	Position of frame $\mathcal{F}_x$ with respect to $\mathcal{F}_y$.
$\boldsymbol{p}_\times^y,\ \omega_\times^y$	Position and angular velocity of object denoted by $\times$, expressed in frame $\mathcal{F}_y$.
$\bar{\boldsymbol{p}}_\times^y$	CoG of object denoted by $\times$, expressed in frame $\mathcal{F}_y$.
$\bar{\boldsymbol{p}}_\times$	CoG of object denoted by $\times$, expressed in frame $\mathcal{F}_M$.
$\bar{\boldsymbol{p}}_i$	CoG of link i expressed in frame $\mathcal{F}_M$.
$(\boldsymbol{p})_x,\ (\boldsymbol{p})_z$	Horizontal and vertical components of $\boldsymbol{p}$.
$L_x^*,\ L_z^*$	Reference horizontal and vertical lengths.
$\tilde{\boldsymbol{p}_x}, \tilde{\boldsymbol{p}_z}$	$\overline{\boldsymbol{p_x}}, \overline{\boldsymbol{p_z}}$ nondimensionalized by $L_x^*,\ L_z^*$.
$\boldsymbol{\Delta p}$	Position difference of $\mathcal{F}_S$ and $\mathcal{F}_B$.
$\psi,\ \theta, \phi$	Yaw-pitch-roll Euler angles.
$\boldsymbol{\Theta}$	Vector of Euler angles.
$R_x^y(\boldsymbol{\Theta}), T_x^y(\boldsymbol{p}, \boldsymbol{\Theta})$	Rotation and transformation matrices of frame $\mathcal{F}_x$ with respect to $\mathcal{F}_y$, defined by $\boldsymbol{\Theta}, \boldsymbol{p}$.
$R_X(\cdot), R_Y(\cdot), R_Z(\cdot)$	Rotation matrices about local X, Y, Z axes.
$T(\boldsymbol{\Theta})$	Mapping of Euler angle rates to angular velocities.
$S(\cdot)$	Skew-symmetric matrix.
$J_{\boldsymbol{x}}^{\boldsymbol{y}}$	Robot Jacobian relating vector $\boldsymbol{x}$ to vector $\boldsymbol{y}$, $\dot{\boldsymbol{y}} = J_{\boldsymbol{x}}\boldsymbol{y}.\boldsymbol{x}$.
$J_{\times,p},\ J_{\times,\omega}$	Robot Jacobians relating joint angle rates to linear and angular velocities, respectively, of object denoted by $\times$.
$\mathcal{T}$	Total kinetic energy of combined system.
$\mathcal{V},\ \mathcal{V}_\mathrm{g}$	Total and gravitational potential energy of combined system.
$\mathcal{L}$	System Lagrangian.
D	Combined system inertia matrix.
B	Combined system viscous damping matrix.
$\kappa,\ \kappa_c$	Combined and slider system stiffness matrices.
$\boldsymbol{c}$	Vector of Coriolis and centrifugal terms of combined system.
q_i	Joint angle of link i.
$\boldsymbol{q}_a, \boldsymbol{q}_p$	Vectors of active and passive manipulator joint angles.
d_c	Counterweight position with respect to slider.
$q_{01,min}, q_{02,min}$	Minimum values of joint angles $q_1,\ q_2$.
ϵ_l, ϵ_u	Lower and upper bounds for allowed aerial manipulator CoG shift.
q_r	Total possible angle range covered by $q_1,\ q_2$.
$\phi_{p_1},\ \omega_{p_1},\ \phi_{p_2}, \omega_{p_2}$	Pulley angles and velocities.
$\boldsymbol{q}_c$	Vector of belt-drive actuated states, which are the counterweight position and pulley angles.
$\tau_m,\ \omega_m,\ V_m,\ i_m$	DC motor torque, angular velocity, input voltage, and current.
$\boldsymbol{x}_n$	Manipulator end-effector task vector.
$\boldsymbol{x}_M$	Manipulator end-effector and CoG task vector.
$\boldsymbol{v}$	Combined system velocity task vector.
$\boldsymbol{\eta}_a, \boldsymbol{\eta}_b$	Vectors of manipulator-slider and hexacopter control variables.
$\boldsymbol{\eta}$	Vector of combined system control variables.
$\boldsymbol{\xi}$	Vector of passive hexacopter variables.
$\boldsymbol{X}$	State vector of combined system.
k_p, k_d, k_i	Discrete PID controller gains.
u_c	Discrete slider control law in the experiment.
$e_c,\ e_\theta$	Slider and tilt angle errors in the experiment.
e_{ss}	Steady-state error of θ in the experiment.
ΔT	Sampling time.
$x[k]$	The value of x at time $k\Delta T$.
$\mu,\ \sigma^2$	Mean and variance of tilt angle time history.
$m_\times$	Mass of object denoted by $\times$.
m_T	Total mass of components.
$L_\times$	Length of object denoted by $\times$.
$I_\times^y$	Inertia tensor of object denoted by $\times$, expressed in frame $\mathcal{F}_y$.
$I_\times$	Inertia tensor of object denoted by $\times$ with respect to CoG of the object.
J_{yy}	Total mass moment of inertia about the base/hexacopter y-axis.
ψ_n	End-effector angle.
ψ_S	Yaw angle of $\mathcal{F}_S$ with respect to $\mathcal{F}_E$.
$d_n,\ L_S$	Brush and solar panel lengths.
$W_b,\ W_S$	Brush and solar panel widths.
α_n	Fixed angle offsetting the brush from the link at the end-effector.
α_S	Solar panel tilt angle.
s	Parametrization variable.
$x_i,\ y_i,\ z_i$	Prescribed end-effector positions at solar panel position i, parametrized by s.
$\boldsymbol{a}_S$	Normal vector to solar panel.

$R_1,\ R_2$	Distance between each of frames $\mathcal{F}_1, \mathcal{F}_2$ with $\mathcal{F}_M$.
$\phi_1,\ \phi_2$	Angle of position vector between each of frames $\mathcal{F}_1, \mathcal{F}_2$ with $\mathcal{F}_M$.
$x_M,\ h_M$	Horizontal and vertical components of $\boldsymbol{p}_B^M$.
$h_1,\ h_2$	Vertical distance between each of frames $\mathcal{F}_1$, $\mathcal{F}_2$ and the lowest point of the hexacopter structure.
r_p	Pulley radius.
$k_1, k_2,\ k_3$	Timing belt stiffness values.
$J_{p_2},\ J_{p_2}$	Pulley mass moments of inertia.
b_c	Counterweight viscous damping coefficient.
$K_t,\ K_e$	DC motor velocity and back emf constants.
R_m	DC motor resistance and inductance.
μ_f	Kinetic friction coefficient between counterweight holder and linear guide rails

Subscripts

d	Control setpoint.
M	Manipulator base.
B	Hexacopter.
BM	Combined manipulator base and hexacopter.
c	Counterweight.
n	end-effector.
s	Slider rails.
S	Solar panel.
M_1, M_2	Servo motors 1 and 2.
b	Brush.
p	Pulley.

Sets

K	Set containing subscripts of all components.
K^*	$K \backslash \{c\}$.
$K_S,\ K_D$	Set containing subscripts of static (S) and dynamic (D) components, $K_S \cup K_D = K$.
$K_M,\ K_c$	Set containing subscripts of manipulator (M) and slider (c) components, $K_M \cup K_c = K_D$.
$\mathcal{Q}_a$	Cartesian product of joint angle limits.
$\mathcal{A}_\mathrm{i}$	Set of joint angles under constraint i.
$\mathcal{A}$	$\cap_{i=1}^{3} \mathcal{A}_\mathrm{i}$.
$\mathcal{W}$	Planar workspace generated by $\boldsymbol{q}_a \in \mathcal{Q}_a$.
$\mathcal{W}_\mathrm{c}$	Planar constrained workspace generated by $\boldsymbol{q}_a \in \mathcal{A}$.

I. INTRODUCTION

The objective of automating laborious, dangerous, repetitive, or time-consuming tasks has been well-met by the use of robotic systems. The construction industry contains many tasks that would fit the aforementioned criteria, including surveying, quality monitoring, and road construction [1], maintenance, and services. For instance, land construction robots have been extensively used for such purposes. In [2], the robots are categorized into construction automation, building maintenance and dismantling, road or bridge construction and maintenance, and other miscellaneous applications. UAVs are also used as an alternative to land robots. Examples are UAVs equipped with a video camera, which are used for surveying [3] and specifically in highway construction [4]. In [5], an approach for motion and torque control of a quadrotor to construct tensile structures with ropes is outlined [1], [2], [6]. A classification scheme of robotics in construction is given in Fig. 1 [7].

One particular application of robotics in construction is the cleaning of special structures and equipment, such as glass and solar panels [8]. In [9], a mobile robot with omni, or multidirectional, wheels was used for the purpose of climbing and cleaning solar panels. Another mobile robot using a roller brush and fans has also been developed for the purpose of solar panel cleaning [10]. In [11], an autonomous mobile robot has been used for this application, and the authors proposed the use of aerial vehicles to overcome the problem of transporting the robot from one panel to another. Due to their extended workspace, aerial manipulators offer an advantage over the limited workspace of mobile robots [12], [13].

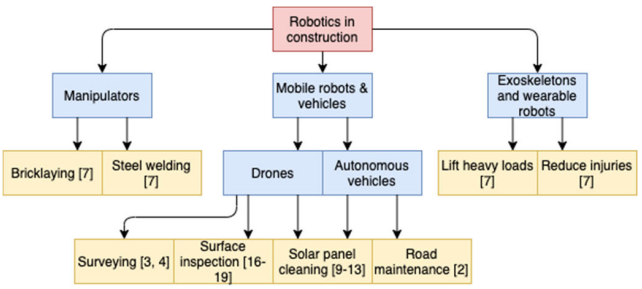

FIGURE 1. Classification scheme for robotics and their applications in construction [7].

Unmanned aerial vehicles (UAVs) are used as an alternative or cooperatively with land robots in construction. Aerial manipulators are proposed to increase the usability of UAVs in this field. Aerial manipulators, which are aerial vehicles equipped with one or more robotic manipulators, are used recently in different areas of research as new applications for quadrotors. In the service industry, aerial manipulators have been used for high-voltage inspection [14], [15], surface contact and maintenance inspection [16], [17], [18], [19], and underground sensor installation [20]. Quadrotors with grippers are used to build cube-like structures in [21] and to assemble a tower composed of foam blocks in [22]. Dual-arm aerial manipulators are designed for bolt-tightening using proper hole localization and torque control in [23] and valve turning in [24]. Another task undertaken by aerial manipulators is the grasping of objects during flight for transport. Specific problems for grasping can concern the shape of the target objects, as explored in [25] and [26], or the problem of grasping moving targets [27], [28]. They have also been used for miscellaneous tasks, such as water [29] and canopy [30] sampling.

One of the main differences among aerial manipulators are owed to the type of robot manipulator they are equipped

with. Typically, these are divided into serial chain and parallel mechanisms, each with varying degrees of freedom (DoF) and workspace. The classification can be further extended to single or multi-arm aerial manipulators. For parallel manipulators, the Delta robot used in [31], [32], [33], and [34] is commonly used. A planar 3 DoF five-bar mechanism is also used [35]. Serial chain robots are used in practically most of the available research on aerial manipulators, such as [36], [37], and [38] for single-arm and [24], [39], [40] for dual-arm.

A common problem that occurs during aerial manipulation is the excessive shift of the system's center of gravity (CoG), inducing instability. The extent of the instability caused by this shift for aerial vehicles is explored in works such as [41], [42], and [43]. In [44], nonlinear controllability is proven for hovering vehicles, although the authors note that the required effort may still be large. Increased control effort may compromise the aerial vehicle's durability. To compensate for this shift, a slider mechanism with counterweight is adopted by some works in the literature. There are also a variety of other methods that do not make use of a slider mechanism.

For those systems that use slider mechanisms, a battery is used as the counterweight during operation, and the differences among their implementations are based on how the counterweight position is specified. In [45], the kinematics yield the system Jacobian that relates the end-effector and horizontal planar CoG to the joints and slider position. The Jacobian is used to dictate the path of the slider for compensation. Other methods, such as [46] and [47], use the mass distribution of the system components to specify the slider position. In addition to the slider, they use the propeller forces to also help compensate the static shift in the CoG. In [48], the counterweight is moved along a linear guide in sync with the motion of the Cartesian base of the robot fitted on the multicopter. Avoiding model-based approaches, [49] uses a classical proportional-derivative-integral (PID) controller to control the position of the counterweight with the objective of zeroing the flight attitude of the quadrotor system.

Compensating for CoG shift without a slider has also been thoroughly explored in the aerial manipulation literature. Methods are typically based on modifying the UAV control scheme to account for manipulator disturbance, designing the manipulator path to minimize the shift, or to embed a structure within the manipulator capable of minimzing the CoG shift. In [50], a combined aerial manipulator dynamic model is presented along with a control scheme based on a transformation that decouples the manipulator and the UAV dynamics. The hexacopter orientation and propeller thrusts are used to stabilize the center of gravity shifts. Feedback linearization is applied to the aerial manipulator dynamics in [51] with rotor thrust inputs to control the center of mass of both the manipulator and the vehicle. For general unknown CoG shifts, a real-time CoG estimation scheme is developed in [52], and the CoG shift values are used in a geometric position controller for the aerial manipulator. Feedback linearization and adaptive controllers have been implemented in the control of multicopters that also take the CoG compensation into account in [53], [54], and [55]. The work in [56] uses the information for position control instead of compensating the CoG. Sliding mode and adaptive controllers have also been designed in [57] for rejection of disturbances, which include the manipulator-induced shift in CoG.

Unconventionally, [58] devised a manipulator path-planning scheme to minimize the shaking force developed from manipulation, thereby preventing the CoG shift rather than treating it. Null-space projection is used to assign a secondary task that reduces the horizontal CoG in [59], resulting in performance improvement in both end-effector error and base displacement in simulations. The same task is assigned in [60] to a cable-suspended aerial manipulator. In the latter, the control inputs are the manipulator joint and winch torques. In [12], the CoG compensation is achieved by design of a parallel robot arm, realized by a pantograph with an end-effector on one end and a counterweight on the other. A novel pantograph-based manipulator with a counterweight is also used in [61]. A prismatic joint located between the UAV and the manipulator is used in [62] to reduce the CoG shift. In [13], a parallel arm design with counterweight is also proposed to ensure the stability of the aerial manipulator during motion of the arms.

In this research, a novel design of a mechatronics system detailing the use of a stable aerial manipulator is proposed for solar panel cleaning. Solar panel arrays are commonly installed on residential or commercial rooftops, as in Fig. 2, making it inconvenient for land robots to perform the cleaning tasks. Sources of instability due to the presence of rough terrain in solar panel fields can also be avoided when employing an aerial robot for the task. Our design, shown in Fig. 3, is inspired by lightweight aerial manipulators, which enjoy the convenience of a large workspace suitable for such applications. By compensating the CoG shift and preventing instability, the workspace of the end-effector is expanded and allows the movement of the cleaning tool both below and in front of the hexacopter. Additionally, since only the motorized brush contributes to the end-effector load, the a priori information of the mass distribution helps the CoG compensation mechanism formulate a static control law to compensate for the shift in CoG with minimal parametric uncertainty. This uncertainty is typically a consequence of the manipulator's payload. Accordingly, the positioning accuracy of the end-effector is increased. We derive a reduced-order model that governs the tilt-angle and slider position dynamics when the hexacopter is hovering, i.e. during a manipulation operation. Feedback linearization is then used to yield a dynamic control law for the slider position, which we show is equivalent to the static control law under certain assumptions.

In this work, we present a comprehensive design scheme that addresses the aforementioned issues in the context of solar panel cleaning, which we consider to be the first step in achieving the final task of efficient solar panel cleaning.

FIGURE 2. Proposed cleaning system positioned above solar panel light installed in a residential location.

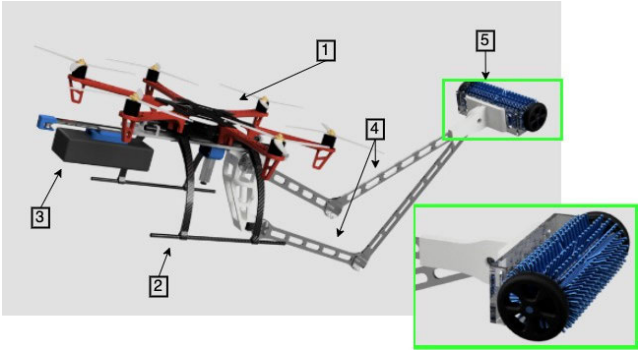

FIGURE 3. CAD model of the proposed aerial manipulator with all components attached. The labeled subsystems are 1) the hexacopter platform and 2) landing gear, 3) the CoG counterbalance mechanism, 4) robot base and links, and 5) end-effector with brush.

The design comprises the restricted manipulator workspace, a path-planning scheme for solar panel cleaning, and the results of a flightless experiment testing the efficacy of the CoG compensation system. A dynamic model governing the hovering condition along with the slider dynamics is also presented.

The contributions of the paper can be summarized as follows: i) Propose a new design of an aerial manipulator, which can be used for solar panel cleaning. ii) For the proposed design, ensure a workspace area that includes the required solar panel surface points without exceeding the limits of the CoG shift. iii) Use the inverse kinematics of the aerial manipulator to formulate a path-planning approach for solar panel cleaning. iv) Derive a reduced order dynamic model that couples the tilt angle and slider position to prove theoretical stability of the aerial manipulator under a dynamic CoG compensation control law. v) Show the efficacy of the compensation mechanism at reducing the tilt angle in an experimental setting.

The remainder of the paper is organized as follows: In section II, the aerial manipulator's design is presented. Modeling is presented in sections III and IV, and control is presented in section V. Experimental results are demonstrated in section VI. Finally, the conclusion and future work is given in section VII.

II. AERIAL MANIPULATOR DESIGN

A. OVERALL SYSTEM

The design of the proposed aerial manipulator with the center of gravity compensation system for solar panel cleaning is shown in Fig. 3, which contains a CAD model of the aerial manipulator with the primary subsystems. The CoG compensation subsystem consists of a slider mechanism with a battery to compensate the variation of the CoG position. In this work, the purpose of the mechanism is to effectively utilize the knowledge of the components' geometric parameters and their masses to robustly counterbalance the mass variation during the manipulator's cleaning operation. The robot arm is selected as a five-bar mechanism with a motorized brush end-effector, which offers the planar DoFs required to operate on the solar panel. The main subsystems are given in Table 1.

TABLE 1. Subsystems comprising the aerial manipulator system with CoG compensation.

System	Description
Carrying platform	*Hexacopter platform*
Manipulator subsystem	*Five-bar mechanism*
CoG compensation mechanism	*Slider mechanism with counterweight (battery)*
Controller subsystem	*Onboard sensors, actuators, and electronics*

B. HEXACOPTER PLATFORM

The selected aerial platform is shown in Fig. 3, which is a DJI F550 hexacopter. The plastic propellers have a diameter of 23.9 cm and a pitch of 10.9 cm. The tip-to-tip distance between two antipodal rotors is 55 cm, or a distance of 15.55 cm between the centers of each rotor and the drone center. The platform has a total height of 8 cm and weighs 850 g, including the propellers and their DC motors [63].

The aerial platform is interfaced with the other subsystems by fitting the landing gear into a custom acrylic rectangular panel that is rigidly attached to the manipulator and slider mechanism. The position of the rectangular panel relative to the hexacopter is adjustable, allowing the manipulator base to be positioned at different distances from its center. The drone is also able to handle a payload consisting of the electronics, manipulator, and cleaning brush.

C. MANIPULATOR SUBSYSTEM

The manipulator subsystem is based on a five-bar mechanism, as shown in Fig. 4. The advantage of this design is to increase the aerial manipulator workspace and keep the actuating motors fixed at the manipulator base [64], thus

preventing further disruption of the CoG location during the motion. The manipulator base is designed with the objective of minimizing the total weight while maintaining structural stability. To achieve this, topology optimization was implemented using Autodesk Fusion 360 [65] to eliminate dead weight from the base while maintaining a reasonable factor of safety. To allow complex shapes to be achieved, the model was designed and built using 3D printing as the primary manufacturing procedure. Additionally, the servo motors were placed horizontally inside the base, which allowed a smaller footprint for the base and thereby reduced its overall weight. The dead weight removal from design and topology optimization resulted in a significant weight drop. Acrylic is used to manufacture the links of the five-bar robot arm. Ball bearings were used to build the joints between the links and the links and the motors.

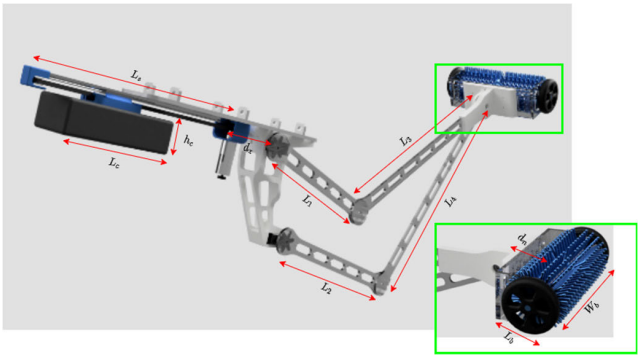

FIGURE 4. CAD model of the manipulator base, and structure allowing it to interface with both the hexacopter and CoG compensation mechanism.

Prior to manufacturing, the thickness and length of each link were designed based on a stress analysis to prevent failure and avoid large deflections under a vertical force applied at the end-effector.

The end-effector of the robot consists of a spin brush. A small DC motor is attached to the rod shaft to provide relative motion between the brush tips and the surface, which is necessary for effective removal of dust and other contaminants.

D. CENTER OF GRAVITY (CoG) COMPENSATION SUBSYSTEM

The center of gravity (CoG) compensation subsystem consists of an active slider mechanism with a counterweight comprising the battery and is shown in Fig. 5. Theoretically, if the slider is sufficiently long, the controlled counterweight can be aptly positioned to zero the shift for any end-effector mass and position. However, since we are restricted by physical limitations, there may exist some end-effector locations which do not allow for the CoG compensation. The primary physical limitation of the slider mechanism is that its length is constrained and cannot provide compensation on both sides of the manipulator. Therefore, the slider and the manipulator were designed to ensure that the maximal forward reach is

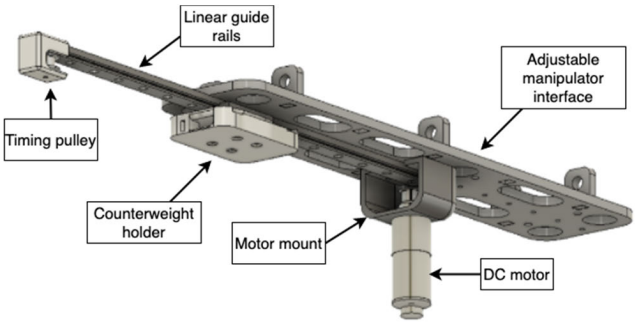

FIGURE 5. CAD model of the proposed CoG compensation mechanism.

compensable, allowing the manipulator to comfortably move within the required workspace. Linear rails are used to guide a moveable acrylic platform mounted with the counterweight. A DC motor-driven belt-drive system uses a timing belt to control the motion.

E. CONTROLLER SUBSYSTEM

Fig. 6 shows a schematic of the hardware/software interfacing and contains the onboard electronics of the proposed system. The feedback sensors are an off-the-shelf DC motor encoder for the slider position and the velocity feedback. Limit switches are installed on the slider mechanism to prevent the counterweight from exceeding the length of the rails. An Adafruit 9-DoF IMU board with built-in sensor fusion is set to retrieve the hexacopter attitude angles and velocities. A battery powered motor driver module is connected to a DC motor to drive the compensation system. Two servo motors with a 30 kg· cm torque drive the active joints. The motion planning and control algorithms are programmed onto an onboard microcontroller (Raspberry Pi 3B+), which is interfaced with the feedback and attitude sensors and provides

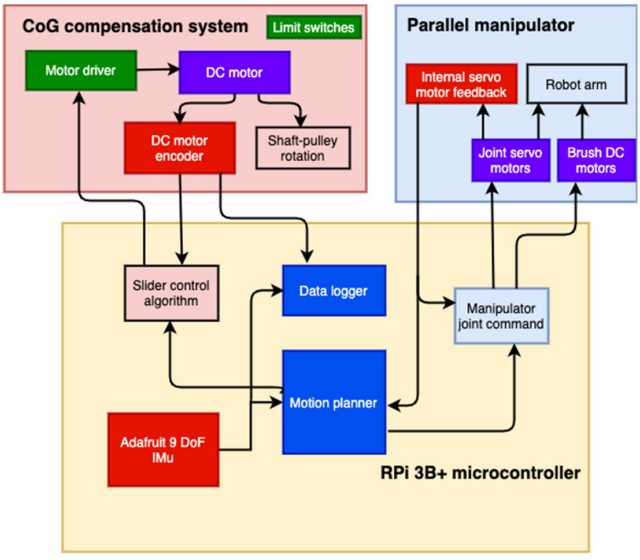

FIGURE 6. General block diagram describing the system.

the control PWM signals to the motor driver and servo motors during operation. To maintain the required levels of current drawn from each actuator, a DC-DC buck converter step down module with a power supply output range of 1.5V to 35V and 3A maximum current is used.

F. ENERGY CONSIDERATIONS

The overall flight time of the proposed system depends primarily on the power required by the drone in two operations: hovering and changing location. The joint servo motors and DC motor to move the counterweight also require energy during operation. For the purpose of this work, the additional power required to move the counterweight is analyzed.

The DC motor used to drive the slider mechanism has a stall torque of $\tau_{stall} = 980\ mN{\cdot}m$ and a zero-load angular velocity of $\omega_{no\ load} = 20\ rpm$. The torque-speed relation is then

$$\tau_m(\omega_m) = 980 - 49\omega_m$$

with ω_m in rpm and τ_m in $mN{\cdot}m$.

The torque required to drive the belt is

$$\tau = \left(m_c g \mu_f\right) r_p,$$

where m_c is the counterweight mass, μ_f is the friction coefficient between the counterweight platform and the timing belt, r_p is the pulley radius, and $g = 9.81\ m/s^2$ is the gravitational acceleration. The pulley radius for the proposed design is $r_p = 6.4\ mm$. Assuming a conservative estimate of $\mu_f = 0.5$ between the rails and the counterweight platform, as well as a total counterweight mass of $m_c = 0.500\ kg$, the required torque is $\tau = 15.7\ mN{\cdot}m$. A conservative estimate of 50% DC motor efficiency yields $\tau_m = 31.4\ mN{\cdot}m$. This corresponds to $\omega_m = 19.36\ rpm$, or a power of $P_m = \tau_m\omega_m = 63.7\ mW$. Compared to the power required by the other components, the power required by the belt-drive system is minimal.

III. SYSTEM MODEL

A. CoG LOCATION

The location of the CoG is calculated as a function of the actuation variables, and the corresponding slider position. The constrained workspace is then shown based on the allowable operating area, which can be sufficiently compensated for by the slider.

Let $\boldsymbol{q} = \left(\boldsymbol{q}_a^T\ \boldsymbol{q}_p^T\right)^T$ denote the vector of joint angles of the five-bar mechanism, where $\boldsymbol{q}_a = \left(q_1\ q_2\right)^T$, and $\boldsymbol{q}_p = \left(q_3\ q_4\right)^T$ are the active and passive joints, respectively. Fig. 7 illustrates the model and reference frames that we adopt for the aerial manipulator. The reference frames of interest are the Earth-fixed frame $\mathcal{F}_E$, the body-fixed hexacopter reference frame $\mathcal{F}_B$, the manipulator body frame $\mathcal{F}_M$, and the joint reference frames $\mathcal{F}_i$ of the ith robot link. In the following, all $\overline{\boldsymbol{p}_\times}$ terms correspond to the CoG of the object specified by subscript $\times$ with respect to $\mathcal{F}_M$.

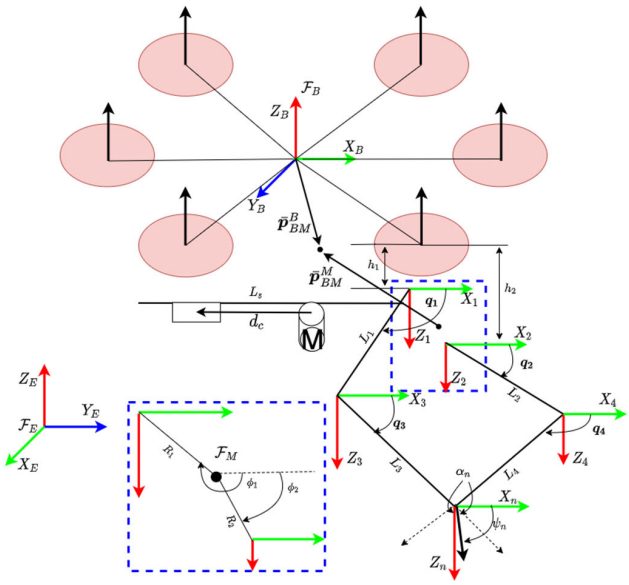

FIGURE 7. Notation and frames used in the aerial manipulator model.

The location of the center of gravity of the combined system with respect to $\mathcal{F}_B$ is denoted by $\bar{\boldsymbol{p}}^B_{BM}(\boldsymbol{q},\ d_c)$, where d_c is the horizontal position of the counterweight measured from the slider starting point. We define K to be the set indicating all components, and we separate it disjointly into static and dynamic component sets K_S, K_D, allowing for easier time differentiation. From Fig. 7, $\bar{\boldsymbol{p}}^B_{BM}(\boldsymbol{q},\ d_c) = \boldsymbol{p}^B_M + \bar{\boldsymbol{p}}^M_{BM}$, which can be expanded as

$$\begin{aligned}\bar{\boldsymbol{p}}^B_{BM}(\boldsymbol{q},\ d_c) &= \boldsymbol{p}^B_M + \frac{\sum_{k\in K} m_k \bar{\boldsymbol{p}}_k}{\sum_{k\in K} m_k} \\ &= \underbrace{\boldsymbol{p}^B_M + \frac{\sum_{k\in K_S} m_k \bar{\boldsymbol{p}}_k}{m_T}}_{\bar{\boldsymbol{p}}_S} + \underbrace{\frac{\sum_{k\in K_D} m_k \bar{\boldsymbol{p}}_k(t)}{m_T}}_{\bar{\boldsymbol{p}}_D},\end{aligned} \tag{1}$$

where $m_T = \sum_{k\in K} m_k$. The CoG positions in (1), expressed in the frame $\mathcal{F}_M$, are denoted by $\bar{\boldsymbol{p}}_k$ for brevity, and the $\bar{\boldsymbol{p}}^M_{BM}$ term is denoted by $\bar{\boldsymbol{p}}$. We adopt this convention for the remainder of this paper. For $k{\in}K_S$, the $\bar{\boldsymbol{p}}_k$ are constants and known a priori, while for $k{\in}K_D$ they are

$$\bar{\boldsymbol{p}}_i = \bar{\boldsymbol{p}}_{M_i} + \frac{L_i}{2}\begin{pmatrix} c_i \\ 0 \\ s_i \end{pmatrix},\ \bar{\boldsymbol{p}}_c = \bar{\boldsymbol{p}}_{M_i} + \begin{pmatrix} -d_x - d_c \\ 0 \\ h_c \end{pmatrix},$$

$$\bar{\boldsymbol{p}}_n = \bar{\boldsymbol{p}}_3 + \frac{L_3}{2}\begin{pmatrix} c_3 \\ 0 \\ s_3 \end{pmatrix} + \frac{d_n}{2}\begin{pmatrix} c_{4+\alpha} \\ 0 \\ s_{4+\alpha} \end{pmatrix},\ \psi_n = q_4 + \alpha_n,$$

$$\bar{\boldsymbol{p}}_{i+2} = \bar{\boldsymbol{p}}_i + \frac{L_i}{2}\begin{pmatrix} c_i \\ 0 \\ s_i \end{pmatrix} + \frac{L_{i+2}}{2}\begin{pmatrix} c_{i+2} \\ 0 \\ s_{i+2} \end{pmatrix},\ i = 1, 2.$$

Here, $c_i = \cos q_i$, $s_i = \sin q_i$, h_c is the vertical distance measured from link 1's base to the counterweight CoG,

the R_i, ϕ_i are the distance and angle from the manipulator base CoG to each of joints 1 and 2.x_M, h_M indicate the horizontal and vertical positions of $\boldsymbol{p}_M^B$. h_1, h_2 are the vertical distances from joint frames $\mathcal{F}_1$, $\mathcal{F}_2$ to the lowest point of the hexacopter structure. α_n is the angle offsetting the brush from the link it is joined to at the end-effector, and d_n is the length of the brush. Table 2 lists the numerical values of the relevant parameters.

We have expressed each component of the position vector of the CoG location with respect to the manipulator base located below the hexacopter. Ideally, the CoG position will remain unchanged as the system performs its required task, i.e. $\bar{\boldsymbol{p}}\left(\boldsymbol{q}(t), d_c(t)\right) = \bar{\boldsymbol{p}}_d$, $\forall t \geq 0$, where $\bar{\boldsymbol{p}}_d$ is the CoG of the unperturbed system at $t = 0$ s. Defining $K^* = K \backslash \{c\}$, the counterweight CoG position can then be set to

$$\bar{\boldsymbol{p}}_{c,d}\left(d_{c,d}(t)\right) = -\frac{1}{m_c}\left[\sum_{k \in K^*} m_k \bar{\boldsymbol{p}}_k - m_T \bar{\boldsymbol{p}}_d\right]. \tag{2}$$

Then, the $\bar{\boldsymbol{p}}_{\boldsymbol{c,d}}$ can be used to solve for the reference slider position $d_{c,d}$ required to compensate for the shift in CoG location. We refer to the slider position obtained in this way as the *static control law*. The slider can attain this position using the motion controller for the slider compensation system. To minimize the shift in $\bar{\boldsymbol{p}}_{BM}^B$, we set the reference as $\bar{\boldsymbol{p}}_d = -\boldsymbol{p}_M^B$.

TABLE 2. Relevant physical parameters of the aerial manipulator.

Component	Mass (g)	Parameter	Value (mm)
m_M	245	x_M	-50
m_1	41.0	L_1	200
m_2	51.3	L_2	250
m_3, m_4	71.0	L_3, L_4	350
m_s	260	L_s	400
m_c, m_n	100, 286	L_c	45.5
m_{M_1}, m_{M_2}	80	h_1, h_2	25, 185
m_T	1285.3	R_1, R_2	54.6, 134.7
		ϕ_1, ϕ_2	230.4°, 61.0°

B. WORKSPACE

We now compute the reachable workspace of the robot manipulator for a fixed UAV position. The planar workspace $\mathcal{W} \subset \mathbb{R}^2$ in the body frame is defined to be the range of the map $\boldsymbol{p}_n\left(\boldsymbol{q}_a\right) : \mathcal{Q}_a \mapsto \mathbb{R}^2$, where $\mathcal{Q}_a = [0,\ 2\pi] \times [0,\ 2\pi]$. However, in practice, the domain of the workspace is subject to several constraints arising from different physical limitations, which we describe in the following subsection.

1) WORKSPACE CONSTRAINTS

The allowed active joint angles $\boldsymbol{q}_a$ will be determined in terms of sets A_k, each of which represents practical constraints. The first constraint is imposed due to the actuated joints $\boldsymbol{q}_a$ being limited by the servo motors having a maximum rotation range of q_r. Thus, $A_1 = \left[q_{0_1,min}, q_{0_1,min} + q_r\right] \times \left[q_{0_2,min}, q_{0_2,min} + q_r\right]$ for starting angles $q_{0_1,min},\ q_{0_2,min}$.

Since the arm is located beneath the UAV structure, we also require that none of the links touch the structure or the rotors during motion. For the actuated and passive links, this translates to

$$A_2 = \{\boldsymbol{q}_a \big| \min\left(R_i s_{\phi_i} + L_i s_i,\ R_i s_{\phi_i} + L_i s_i + L_{i+2} s_{i+2}\right) > -h_i,\ i = 1, 2\}. \tag{3}$$

The third constraint is due to the allowable shift in the center of gravity position. We require that the workspace does not include locations that the slider mechanism cannot balance. Due to the slider length L_s, the slider position is restricted to $d_c(t) \in \left[\frac{L_c}{2},\ L_s - \frac{L_c}{2}\right]$. With this and d_c^* obtained from (2),

$$d_c = f\left(d_c^*\right) = \begin{cases} \frac{L_c}{2}, & d_c^* \in \left(-\infty, \frac{L_c}{2}\right] \\ d_c^*, & d_c^* \in \left(\frac{L_c}{2},\ L_s - \frac{L_c}{2}\right] \\ L_s - \frac{L_c}{2}, & d_c^* \in \left(\frac{L_c}{2},\ \infty\right). \end{cases} \tag{4}$$

Due to the limitations, some areas in the otherwise reachable workspace are deemed restricted if the horizontal component $\bar{p}_x$ of $\bar{\boldsymbol{p}}$ exceeds some imposed lower and upper bounds $\varepsilon_l,\ \varepsilon_u$. Then, $A_3 = \left\{\boldsymbol{q}_a | \bar{p}_x \in [\varepsilon_l,\ \varepsilon_u],\ d_c = f\left(d_c^*\right)\right\}$.

Using the sets A_k, the constrained workspace $\mathcal{W}_c \subset \mathcal{W}$ is defined to be the range of the restriction of $\bar{\boldsymbol{p}}_n\left(\boldsymbol{q}_a\right)$ over $\mathcal{Q}_a \bigcap \mathcal{A}$, and $\mathcal{A} = \bigcap_{k=1}^{3} A_k$. In other words, this is the set of possible end-effector locations with restricted domain on the active joint angles as defined by the constraints.

2) MANIPULATOR WORKSPACE OPTIMIZATION

To simulate the workspace, the horizontal position of the CoG reference is chosen to be $\bar{p}_x = x_M$, which is the horizontal distance between the manipulator and hexacopter bases. The workspace is studied for $x_M = 0$ mm and $x_M = -50$ mm, representing the cases in which the manipulator base is located either directly below the hexacopter or 50 mm ahead.

We simulate these conditions with and without the slider mechanism to compare the workspace gained using the mechanism. Fig. 8 shows the constrained planar workspace of the parallel manipulator with the allowed CoG shift in position of $\varepsilon_1 = 20$ mm, where $\varepsilon_l = \varepsilon_u = \varepsilon_i$. The servo joint angle range is $q_r = \pi$ rad, and $\left(q_{0_1,min},\ q_{0_2,min}\right) = (0,\ 0)$ rad.

Fig. 8 illustrates how changing the horizontal position of the manipulator with respect to the hexacopter base increases the allowed workspace. When $x_M = 0$ mm, the end-effector is restricted from moving left, since it will sooner reach the vicinity of the slider mechanism and the shift in CoG location will be out-of-bounds on the left. When $x_M = 50$ mm, there is more flexibility to move leftwards, since the reference CoG is also set to the left.

The workspace of the manipulator without a slider is heavily restricted in the forwards motion. The configuration space after adding the slider has a larger area and placing the manipulator at $x_M = 50$ mm further increases it.

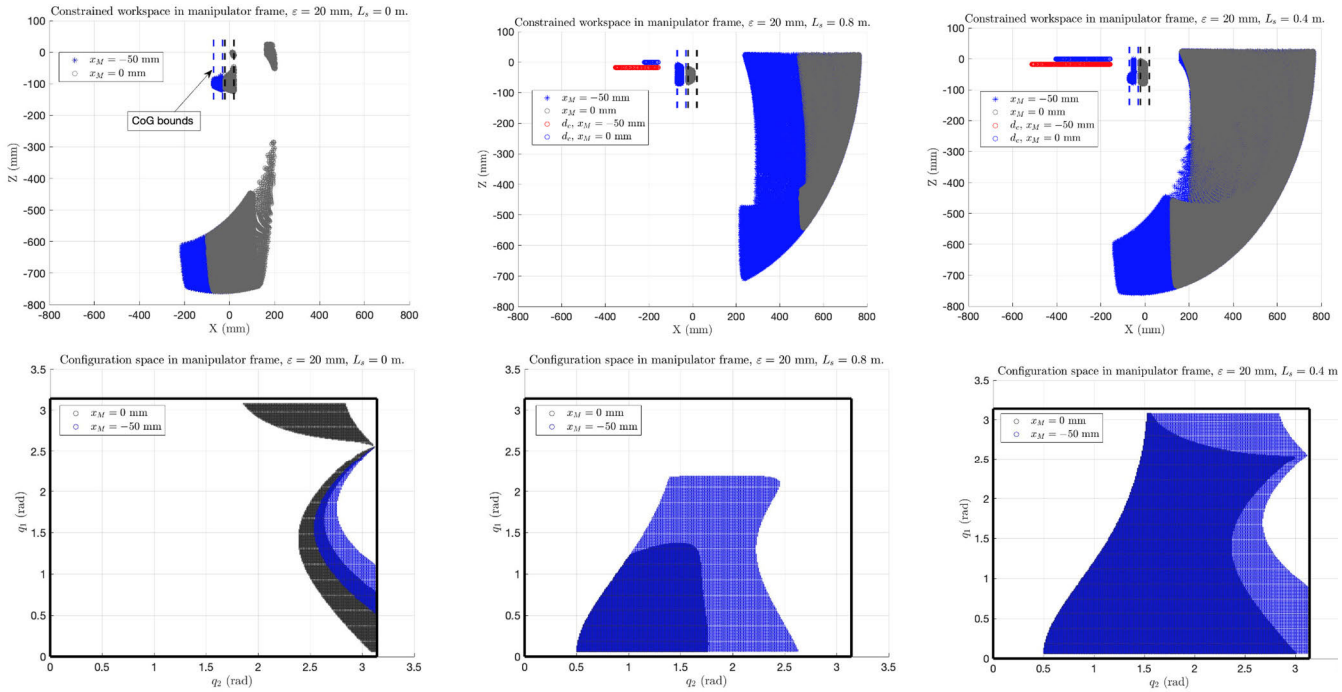

FIGURE 8. Constrained planar workspace and configuration space for the proposed manipulator, simulated without the CoG compensation mechanism (leftmost figures), and for slider lengths of 800 mm (middle figures) and 400 mm (rightmost figures).

Furthermore, when the slider length $L_s = 400$ mm, the configuration space is further expanded, and allows the extended motion of the manipulator to the bottom. Since the counterweight and slider are effective at compensating the gravity effect during the forward operation of the manipulator, shortening the length of the slider is desirable to prevent tipping on the left. The slider mechanism compensation greatly improves the forward reach of the robot arm by about 450-600 mm, depending on the ε bounds chosen for the CoG shift. Based on this discussion, the shorter slider is chosen, with the manipulator placed ahead of the hexacopter base.

Fig. 9 shows the planar workspace and configuration space of the setup used in the experiments, with $\varepsilon = 20$ mm, $L_s = 400$ mm, and $x_M = 50$ mm. The allowable regions of operation are represented by the blue regions. Furthermore, near-singularity regions are identified. These are high-torque regions of the configuration space where the load torques on one of the joints exceeds the motor's capacity, which occurs close to $q_3 = q_4$.

IV. MODELING: KINEMATICS AND DYNAMICS

Since the operating mode in this work is mainly a manipulator cleaning operation for solar panels while hovering, we begin first by describing the kinematics of the manipulator, followed by the combined aerial manipulator kinematics. The latter is necessary to suitably position the hexacopter for the robot's constrained workspace to intersect with the solar panel region of interest. Finally, the system dynamics is used to model the effect of the end-effector contact with the panel surfaces, as well as the coupled dynamics of the hexacopter and the robot arm.

A. KINEMATICS

1) KINEMATICS IN THE BODY FRAME

To describe the manipulator kinematics with respect to $\mathcal{F}_B$, let $T_n^B(\boldsymbol{q}) = T_M^B T_n^M(\boldsymbol{q})$ be the transformation matrix relating the end-effector frame $\mathcal{F}_n$ to $\mathcal{F}_B$. The transformation T_M^B consists of only an identity rotation and the constant translation $\boldsymbol{p}_M^B$. For open kinematic chains, $T_n^M(\boldsymbol{q})$ is the product of the intermediate manipulator joint transformations. The closed-chain direct kinematics is somewhat more involved and dependent on the design, and in this paper the details for the five-bar manipulator with end-effector tool are shown. $T_n^M(\boldsymbol{q})$ is given by

$$T_n^M(\boldsymbol{q}) = \begin{pmatrix} R_Y(\psi_n) & \bar{\boldsymbol{p}}_n + \frac{d_n}{2}\begin{pmatrix} c_{\psi_n} \\ 0 \\ -s_{\psi_n} \end{pmatrix} \\ \mathbf{0}_{1\times 3} & 1 \end{pmatrix}, \tag{5}$$

where $R_Y(\psi_n)$ is a rotation about the y-axis and $\psi_n = q_4 + \alpha_n$ is the end-effector angle. Kinematics of standard five-link robot manipulators are detailed in [66] and [67].

For given input angles $\boldsymbol{q}_a$, the $\boldsymbol{q}_p$ are determined using the kinematic constraint, thereby completely specifying $T_n^M(\boldsymbol{q})$. We follow a typical analytical method to compute the $\boldsymbol{q}_p$ based on [68]. For simplicity, the closed-chain kinematic constraint for the 5-bar mechanism (Fig. 7) can be written

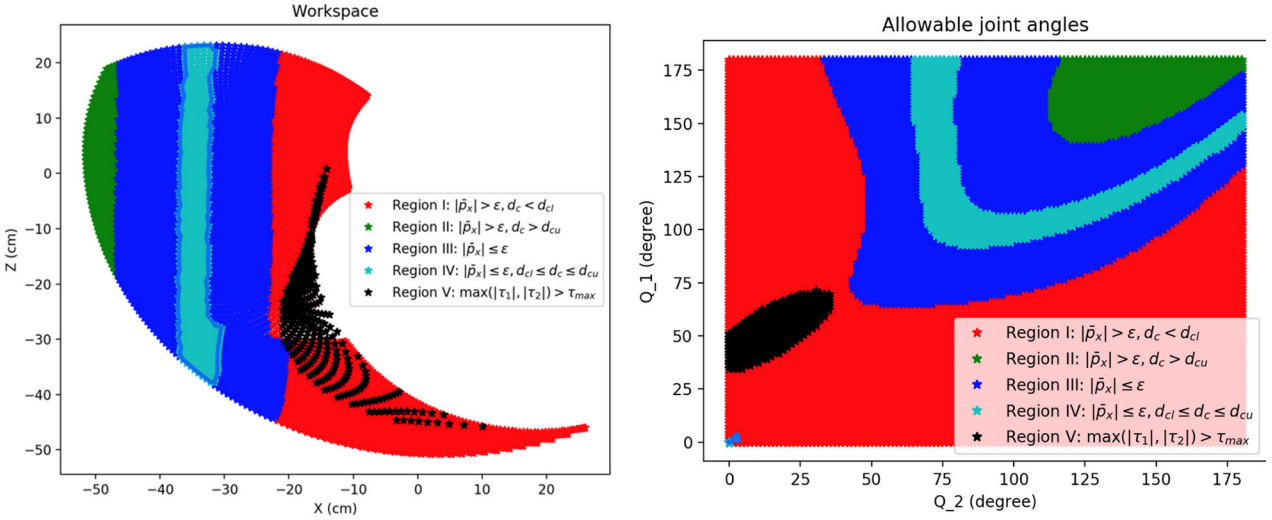

FIGURE 9. Workspace and configuration space of the chosen setup, with $L_s = 400$m and $x_M = -50$mm. High-torque regions are better avoided to reduce power demand on the servo.

with reference to $\mathcal{F}_1$ as follows:

$$L_1 e^{jq_1} + L_3 e^{jq_3} = Re^{j\phi} + L_2 e^{jq_2} + L_4 e^{jq_4}, \tag{6}$$

where

$$R = \sqrt{R_1^2 + R_2^2 - 2R_1 R_2 \cos(\phi_1 - \phi_2)},$$
$$\phi = \frac{R_2 s_{\phi_2} - R_1 s_{\phi_1}}{R_2 c_{\phi_2} - R_1 c_{\phi_1}}.$$

$R,\ \phi$ represent the distance and angle from $\mathcal{F}_1$ to $\mathcal{F}_2$.

By isolating the terms containing q_4 in (6) and equating the sum of squares of the real and imaginary equations, we can then isolate the terms containing q_3. We also do this for q_3 followed by q_4, yielding the two equations for $i = 1,\ 2$

$$(-1)^i (\gamma_1 c_{i+2} + \gamma_2 s_{i+2}) = \frac{1}{L_{i+2}} (\alpha + \beta_i), \tag{7}$$

where

$$\gamma_1 = L_1 c_1 - L_2 c_2 - R c_\phi, \quad \gamma_2 = L_1 s_1 - L_2 s_2 - R s_\phi,$$
$$\alpha = \frac{1}{2}\left(R^2 + L_1^2 + L_2^2\right) + RL_2 c_{\phi,2} - RL_1 c_{\phi,\,1} - L_2 L_1 c_{1,2},$$
$$\beta_i = (-1)^i \frac{L_4^2 - L_3^2}{2}.$$

here, $c_{1,2} = \cos(\theta_1 - \theta_2)$ for some angles $\theta_1,\ \theta_2$. Equations of the form in (7) can be solved by substituting $c_i = \frac{1-u_i^2}{1+u_i^2},\ s_i = \frac{2u_i}{1+u_i^2}$ for $i = 3,\ 4$. By solving the resulting quadratics in $q_3,\ q_4$ and noting that $\gamma_1^2 + \gamma_2^2 = 2\alpha$, we get

$$u_{i+2} = \frac{(-1)^i L_{i+2}\gamma_2 \pm \sqrt{2L_{i+2}^2\alpha - (\alpha + \beta_i)^2}}{(-1)^i L_{i+2}\gamma_1 + (\alpha + \beta_i)}, \tag{8}$$

and the $q_{i+2} = 2\tan^{-1}(u_{i+2})$ for $i = 1,\ 2$. From this, the end-effector position and orientation can be obtained using (5).

The inverse kinematics problem is defined by finding the active joint angles $\boldsymbol{q}_a$ that yield the given pose prescribed by the end-effector task vector $\boldsymbol{x}_n = \begin{pmatrix}\boldsymbol{p}_n^T & \psi_n\end{pmatrix}^T$ with respect to $\mathcal{F}_M$. The active pair $\boldsymbol{q}_a$ can position the end-effector as desired, resulting in the orientation $\psi_n = q_4 + \alpha_n$. If only the end-effector coordinates $\boldsymbol{p}_n = \begin{pmatrix}a & y_0 & b\end{pmatrix}^T$ are required, then the loop equations are

$$R_1 c_{\phi_1} + L_1 c_1 + L_3 c_3 = R_2 c_{\phi_2} + L_2 c_2 + L_4 c_4 = a,$$
$$R_1 s_{\phi_1} + L_1 s_1 + L_3 s_3 = R_2 s_{\phi_2} + L_2 s_2 + L_4 s_4 = -b. \tag{9}$$

By isolating the terms containing q_3 and q_4 in each pair of equations and summing the squares, we can solve for q_1 and q_2 with methods similar to the solution of (7). The solutions are $q_i = 2\tan^{-1}(u_i)$ for $i = 1,\ 2$, where the u_i are given by

$$u_i = \frac{b_i' \pm \sqrt{b_i'^2 + a_i'^2 - L_i'^2}}{a_i' + L_i'}, \quad a_i' = a - R_i c_{\phi_i},$$
$$b_i' = b - R_i s_{\phi_i}, \quad L_i' = \frac{a_i'^2 + b_i'^2 + L_i^2 - L_{i+2}^2}{2L_i}. \tag{10}$$

q_3 and q_4 can be recovered directly by substituting the solutions into (9) (or, alternatively, using the forward kinematics solution (8)). There are eight inverse kinematics configurations for one end-effector position, attained by switching the plus/minus sign in (10) for $i = 1,\ 2$, and a choice of elbow up/down for the $\boldsymbol{q}_p$ as seen earlier in the forward kinematics. Finally, for a given slider position d_c, the body-frame CoG $\bar{p}_x$ can be found by substituting the $\boldsymbol{q}$ and d_c into (1).

When the end-effector orientation is also required, as is the case when equipped with the brush to aptly clean the solar panel surface, then the angle α_n should be added as a joint angle resulting in an additional DoF. In this case, the inverse kinematics problem becomes that of realizing both $\boldsymbol{p}_n,\ \psi_n$ using $\begin{pmatrix}\boldsymbol{q}_a^T & \alpha_n\end{pmatrix}^T$. The solution to this problem is identical to

the solution given by (10) above, and $\alpha_n = \psi_n - q_4$ can be used to achieve the desired orientation.

2) AERIAL MANIPULATOR KINEMATICS

Consider again the frames defined in Fig. 7. The position $\boldsymbol{p}_B^E$ and orientation $\boldsymbol{\Theta}_B$ of the hexacopter with respect to $\mathcal{F}_E$ are given at all times by $\boldsymbol{p}_B^E = \begin{pmatrix} p_x & p_y & p_z \end{pmatrix}^T$, $\boldsymbol{\Theta}_B = \begin{pmatrix} \psi & \theta & \phi \end{pmatrix}^T \in \mathbb{R}^3$, which are the Cartesian coordinates and Euler angles. The UAV pose in $\mathcal{F}_E$ is described by $T_B^E\left(\boldsymbol{p}_B^E,\ \boldsymbol{\Theta}_B\right) \in \mathbb{R}^{4\times4}$ [69], where

$$T_B^E\left(\boldsymbol{p}_B^E,\ \boldsymbol{\Theta}_B\right) = \begin{pmatrix} R_B^E\left(\boldsymbol{\Theta}_B\right) & \boldsymbol{p}_B^E \\ \boldsymbol{0} & 1 \end{pmatrix},$$

and $R_B^E\left(\boldsymbol{\Theta}_B\right)$ is the rotation matrix defined by Euler angles. The end-effector frame $\mathcal{F}_n$ with respect to $\mathcal{F}_E$ is given by the transformation

$$T_n^E\left(\boldsymbol{p}_B^E,\ \boldsymbol{\Theta}_B, \boldsymbol{q}_a\right) = T_B^E\left(\boldsymbol{p}_B^E,\ \boldsymbol{\Theta}_B\right) T_n^B\left(\boldsymbol{q}\right). \tag{11}$$

From (11), we have that

$$\begin{aligned} \boldsymbol{p}_n^E &= \boldsymbol{p}_B^E + R_B^E \boldsymbol{p}_n^B, \\ R_n^E &= R_B^E R_n^B. \end{aligned}$$

Here, $\boldsymbol{p}_n^B = \boldsymbol{p}_M^B + \boldsymbol{p}_n^M$. The manipulator control variables, as defined earlier, are $\boldsymbol{x}_a = \begin{pmatrix} \boldsymbol{q}_a^T & d_c \end{pmatrix}^T$, and the hexacopter control variables are $\boldsymbol{x}_b = \begin{pmatrix} \boldsymbol{p}_B^{E\,T} & \psi \end{pmatrix}^T$.

3) DIFFERENTIAL KINEMATICS

Let $\boldsymbol{\eta}_a = \begin{pmatrix} \boldsymbol{q}_a^T & d_c \end{pmatrix}^T$ be the vector of actuated degrees of freedom and the total task vector $\boldsymbol{x}_M = \begin{pmatrix} \boldsymbol{x}_n^T & \bar{\boldsymbol{p}} \end{pmatrix}^T$ consist of the end-effector task vector as defined in the body-frame kinematics, and the manipulator's CoG position. The differential kinematics is described by $\dot{\boldsymbol{x}}_M = J_{\boldsymbol{\eta}_a}^{\boldsymbol{x}_M} \dot{\eta}_a$, where

$$J_{\boldsymbol{\eta}_a}^{\boldsymbol{x}_M} = \begin{pmatrix} J_{\boldsymbol{q}_a}^{\boldsymbol{x}_n} & \boldsymbol{0}_{4\times1} \\ J_{\boldsymbol{q}_a}^{\bar{\boldsymbol{p}}} & J_{d_c}^{\bar{\boldsymbol{p}}} \end{pmatrix}.$$

(6) can be written as the kinematic constraint $F\left(\boldsymbol{q}\right) = 0$, which induces the differential relation $\dot{\boldsymbol{q}}_p = J_{\boldsymbol{q}_a}^{\boldsymbol{q}_p} \dot{\boldsymbol{q}}_a$, and

$$J_{\boldsymbol{q}_a}^{\boldsymbol{q}_p} = -\left[\frac{\partial F}{\partial \boldsymbol{q}_p}\right]^{-1} \frac{\partial F}{\partial \boldsymbol{q}_a} = \frac{1}{L_3 L_4 s_{3,4}} \begin{pmatrix} -L_1 L_4 s_{1,4} & L_2 L_4 s_{2,4} \\ -L_1 L_3 s_{1,3} & L_2 L_3 s_{2,3} \end{pmatrix}.$$

The Jacobian $J_{\boldsymbol{q}_a}^{\boldsymbol{x}_n}(\boldsymbol{q})$ of the end-effector twist $\dot{\boldsymbol{x}}_n$ can then be obtained

$$J_{\boldsymbol{q}_a}^{\boldsymbol{x}_n}\left(\boldsymbol{q}\right) = \frac{\partial \boldsymbol{x}_n}{\partial \boldsymbol{q}_a} + \frac{\partial \boldsymbol{x}_n}{\partial \boldsymbol{q}_p} J_{\boldsymbol{q}_a}^{\boldsymbol{q}_p} = \frac{1}{s_{3,4}} \begin{pmatrix} L_1 s_{4} s_{1,3} & -L_2 s_3 s_{2,4} \\ 0 & 0 \\ -L_1 c_4 s_{1,3} & L_2 c_3 s_{2,4} \\ -\frac{L_1}{L_3} s_{1,4} & \frac{L_2}{L_3} s_{2,4} \end{pmatrix}.$$

Using the definition from (1),

$$\frac{d}{dt}\bar{\boldsymbol{p}} = \frac{1}{m_T}\left[\sum_{i=1}^{4} m_i \left(\frac{\partial \bar{\boldsymbol{p}}_i}{\partial \boldsymbol{q}_a} + \frac{\partial \bar{\boldsymbol{p}}_i}{\partial \boldsymbol{q}_p} J_{\boldsymbol{q}_a}^{\boldsymbol{q}_p}\right) + m_e E_{13} J_{\boldsymbol{q}_a}^{\boldsymbol{x}_n}\right] \dot{\boldsymbol{q}}_a + \frac{\partial \bar{\boldsymbol{p}}_i}{\partial \bar{\boldsymbol{p}}_c} \frac{\partial \bar{\boldsymbol{p}}_c}{\partial d_c} \dot{d}_c.$$

We use $E_{a_1,\ldots,a_n} \in \mathbb{R}^{n\times m}$ to denote the selection matrix used to extract a desired submatrix. It consists of 1s in the a_i^{th} position for each row i and 0s everywhere else. Its inner dimension m is determined by imposing well-defined matrix multiplication. By computing the derivatives using the definition of $\bar{\boldsymbol{p}}$, defining the quantities $m'_E = m_3 + m_4 + 2m_n$, $m'_1 = m_1 + m_3$, $m'_2 = m_2 + m_4$ and simplifying, we get $J_{d_c}^{\bar{\boldsymbol{p}}} = \frac{m_c}{m_T}\begin{pmatrix} -1 \\ 0 \end{pmatrix}$ and (12), as shown at the bottom of the next page.

When our primary task is the control of the planar end-effector position and the x-component of the position of the CoG, the associated Jacobian is $J_{\boldsymbol{\eta}_a}^{\boldsymbol{p}_n,\ \bar{p}_x} = E_{135} J_{\boldsymbol{x}_a}^{\boldsymbol{x}_M} \in \mathbb{R}^{3\times3}$.

The differential kinematics of the combined system can be realized by using the time derivatives of the end-effector position, orientation, and x-CoG. We note the property [70]

$$\dot{R}_B^E \boldsymbol{p}_n^B = S\left(\boldsymbol{\omega}_B^E\right) R_B^E \boldsymbol{p}_n^B = -S\left(R_B^E \boldsymbol{p}_n^B\right) \boldsymbol{\omega}_B^E,$$

where $S\left(\cdot\right) \in \mathbb{R}^{3\times3}$ is the skew-symmetric matrix representing the cross-product operator. The derivatives are given by [70]

$$\begin{aligned} \dot{\boldsymbol{p}}_n^E &= \dot{\boldsymbol{p}}_B^E - S\left(R_B^E \boldsymbol{p}_n^B\right) \boldsymbol{\omega}_B^E + R_B^E E_{123} J_{\boldsymbol{q}_a}^{\boldsymbol{x}_n} \dot{\boldsymbol{q}}_a, \\ \boldsymbol{\omega}_n^E &= \boldsymbol{\omega}_B^E + R_B^E \boldsymbol{\omega}_n^B, \\ \dot{\bar{p}}_x &= E_1 \left[J_{\boldsymbol{q}_a}^{\bar{p}_x} \dot{\boldsymbol{q}}_a + J_{dc}^{\bar{p}_x} \dot{d}_c\right]. \end{aligned} \tag{13}$$

Since the angular velocities $\boldsymbol{\omega}_n^E, \boldsymbol{\omega}_B^E$ are commonly specified by Euler angles, they are related by $\boldsymbol{\omega} = T(\boldsymbol{\Theta})\dot{\boldsymbol{\Theta}}$, where [70]

$$T\left(\boldsymbol{\Theta}\right) = \begin{pmatrix} 0 & -s_\psi & c_\psi c_\theta \\ 0 & c_\psi & s_\psi c_\theta \\ 1 & 0 & -s_\theta \end{pmatrix}.$$

Defining $\boldsymbol{v}_{\mathbf{n}}^{\mathbf{E}} = \begin{pmatrix} \dot{\boldsymbol{p}}_n^{E\,T} & \boldsymbol{\omega}_n^{E\,T} & \dot{\bar{p}}_x \end{pmatrix}^{\mathbf{T}}$, we can rewrite (13) as

$$\boldsymbol{v}_n^E = \begin{pmatrix} \boldsymbol{I}_3 & -S\left(R_B^E \boldsymbol{p}_n^B\right) T\left(\boldsymbol{\Theta}_B\right) & R_B^E E_{123} J_{\boldsymbol{q}_a}^{\boldsymbol{x}_n} & \boldsymbol{0}_{3\times1} \\ \boldsymbol{0}_3 & T\left(\boldsymbol{\Theta}_B\right) & R_B^E E_{242} J_{\boldsymbol{q}_a}^{\boldsymbol{x}_n} & \boldsymbol{0}_{3\times1} \\ \boldsymbol{0}_{1\times3} & \boldsymbol{0}_{1\times3} & E_1 J_{\boldsymbol{q}_a}^{\bar{\boldsymbol{p}}} & E_1 J_{d_c}^{\bar{\boldsymbol{p}}} \end{pmatrix} \times \begin{pmatrix} \dot{\boldsymbol{p}}_B^E \\ \dot{\boldsymbol{\Theta}}_B \\ \dot{\boldsymbol{q}}_a \\ \dot{d}_c \end{pmatrix}. \tag{14}$$

Since $\dot{\phi}, \dot{\theta}$ are not control variables, we can write $\boldsymbol{v}_n^E = J_{\boldsymbol{\eta}}\dot{\boldsymbol{\eta}} + J_{\boldsymbol{\xi}}\dot{\boldsymbol{\xi}}$, where $\boldsymbol{\eta} = \begin{pmatrix} \boldsymbol{x}_b^T & \boldsymbol{x}_a^T \end{pmatrix}^T$, $\boldsymbol{\xi} = \begin{pmatrix} \phi & \theta \end{pmatrix}^T$. $J_{\boldsymbol{\eta}}, J_{\boldsymbol{\xi}}$ can be extracted from the total Jacobian in (14) by retrieving the associated columns for the active and passive degrees of freedom.

4) INVERSE KINEMATICS AND PATH-PLANNING

In general, if the desired end-effector position $\boldsymbol{p}_{n,d}$ and orientation $\boldsymbol{\Theta}_{n,d}$ are fully specified in $\mathbb{R}^6$, the active control variables $\boldsymbol{\eta}$ are sufficient to achieve the desired pose. The yaw angle ψ and the $\boldsymbol{q}_a$ can be used to achieve $\boldsymbol{\Theta}_{n,d}$, and $\boldsymbol{p}_{n,d}$ can be freely accounted for using the hexacopter position $\boldsymbol{p}_B^E$.

When closed-form solutions are not available, well-known inverse kinematics algorithms (e.g. in [71]) that use the Jacobian can be employed to compute $\boldsymbol{\eta}$ for a given pose.

In this work, since we only require the end-effector position and z-axis to be specified, a different strategy is proposed that takes into account the CoG position compensation using the constrained workspace described in Section III-B1. The procedure is described for a single solar panel at some fixed location and orientation.

We denote by $\mathcal{F}_S$ the frame with origin assigned to the bottom left corner of the panel, where Z_S is aligned with the Earth Z_E and X_S points along the width of the panel, shown in Fig. 10.

The hexacopter degrees of freedom are used to situate the aerial manipulator at a suitable position above the panel, and the manipulator sweeps the brush along the inclined length of the panel. In the following, the latter process will be referred to as a stroke. We assume that during hovering a) the manipulator can access the length of the panel, and b) the shift in CoG location can be suitably compensated for the entirety of one stroke.

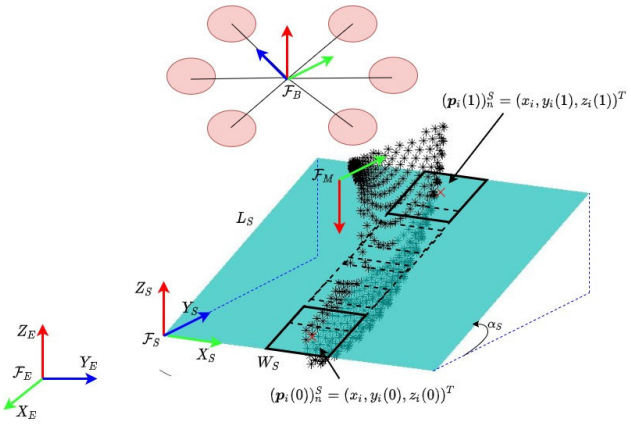

FIGURE 10. Constrained manipulator workspace during cleaning operation, with $\Delta P_y = 0.5$m, $\Delta P_z = 0.675$m.

The aforementioned, then, consists of defining T_B^E to position and orient the hexacopter above the panel and specifying the desired end-effector locations in the panel frame using T_n^S. T_S^E is fixed and known based on the solar panel. Since $T_n^E = T_S^E T_n^S = T_B^E T_n^B$, we have that

$$T_n^M = \left(T_M^E\right)^{-1} T_S^E T_n^S, \tag{15}$$

and the $\boldsymbol{q}_a$ are then obtained using the body-frame inverse kinematics.

The transformations for frames $\mathcal{F}_S$ and $\mathcal{F}_M$ are

$$T_S^E = \begin{pmatrix} R_z(\psi_s)\, \boldsymbol{p}_S \\ \mathbf{0} \quad 1 \end{pmatrix}, \; T_M^E = \begin{pmatrix} R(\boldsymbol{\Theta})\, \boldsymbol{p}_B^E + \boldsymbol{p}_M^B \\ \mathbf{0} \quad 1 \end{pmatrix}, \tag{16}$$

where $\mathcal{F}_S$ is known a priori. To orient the aerial manipulator to face the panel as in Fig. 10, we set $\psi = \psi_s + \frac{\pi}{2}$ and $\boldsymbol{p}_B^E = \boldsymbol{p}_S + \Delta\boldsymbol{p}$ for some displacement $\Delta\boldsymbol{p}$ from the panel frame, to be determined. The choice of $\Delta\boldsymbol{p}$ will be such that the desired end-effector locations are contained in the constrained workspace $\mathcal{W}_c$.

The desired end-effector positions $(\boldsymbol{p}_i)_n^S$ at the center of the brush tip are given by the line segments $(\boldsymbol{p}_i)_n^S = \begin{pmatrix} x_i & y_i(s) & z_i(s) \end{pmatrix}^T$, parameterized by $s \in [0,\ 1]$. Since the brush width W_b may not perfectly divide the panel width W_S, then $\frac{W_S}{W_b} = n - 1 + \frac{W_b - W_e}{W_b}$ for some $W_e < W_b$. If we define $x_i = \frac{W_b}{2} + (i-1)\left(W_b - \frac{W_e}{n-1}\right)$ for $i = 1, \ldots, n$, then the brush will traverse the panel width. The line segments are parameterized by

$$y_i(s) = \begin{cases} \left[\frac{d_n}{2} + (L_S - d_n)\, s\right] c_{\alpha_s} & i \text{ odd} \\ \left[\frac{d_n}{2} s + \left(L_S - \frac{d_n}{2}\right)(1-s)\right] c_{\alpha_s} & i \text{ even} \end{cases}$$
$$z_i(s) = \tan(\alpha_S)\, y_i(s). \tag{17}$$

The odd and even i separate the paths into strokes moving from the bottom to the top of the panel and vice versa, respectively.

The center of brush tip should also be tangent to the panel surface at all times. This is achieved by setting the approach vector $\boldsymbol{a}_S$ of the end-effector to the normal vector of the panel surface, i.e. $\boldsymbol{a}_S = \begin{pmatrix} 0 & s_{\alpha_S} & -c_{\alpha_S} \end{pmatrix}^T$. Using this orientation and the $(\boldsymbol{p}_i)_n^S$,

$$\left(T_n^S\right)_i = \begin{pmatrix} (R_i)_n^S & (\boldsymbol{p}_i)_n^S \\ \mathbf{0} & 1 \end{pmatrix}, \; (R_i)_n^S = \begin{pmatrix} 0 & -1 & 0 \\ c_{\alpha_S} & 0 & -s_{\alpha_S} \\ s_{\alpha_S} & 0 & c_{\alpha_S} \end{pmatrix}. \tag{18}$$

Given the above, we return to the problem of specifying $\Delta\boldsymbol{p}$ to ensure that the manipulator's plane of operation intersects the line segments described in (17). By substituting (16) and (18) into (15), we obtain

$$\left(T_n^M\right)_i = \begin{pmatrix} R_z^T\left(\frac{\pi}{2}\right)(R_i)_n^S & (\boldsymbol{p}_i)_n^M \\ \mathbf{0} & 1 \end{pmatrix},$$
$$(\boldsymbol{p}_i)_n^M = R_z^T\left(\frac{\pi}{2}\right)\left[(\boldsymbol{p}_i)_n^S - R_z^T(\psi_S)\, \Delta\boldsymbol{p}\right].$$

The orientation is computed by $\left(R_n^M\right)_i = R_z^T\left(\frac{\pi}{2}\right)(R_i)_n^S = R_Y^T(\alpha_S)$, which corresponds to an end-effector orientation of $\psi_n = \alpha_S$ in the body frame.

To make the choice of $\Delta\boldsymbol{p}$, we require a) the y-component of each $(\boldsymbol{p}_i)_n^M$ to vanish (planar manipulator), and b) the other two components to be contained in $\mathcal{W}_c$. Denoting the

$$J_{\boldsymbol{q}_a}^{\bar{\boldsymbol{p}}} = \frac{1}{2m_T s_{3,4}} \begin{pmatrix} L_1\left(-m_1' s_1 s_{3,4} + m_E' s_4 s_{1,3}\right) & L_2\left(m_2' s_2 s_{3,4} + m_E' s_3 s_{2,4}\right) \\ L_1\left(m_1' c_1 s_{3,4} - m_E' c_4 s_{1,3}\right) & L_2\left(m_2' c_2 s_{3,4} + m_E' c_3 s_{2,4}\right) \end{pmatrix} \tag{12}$$

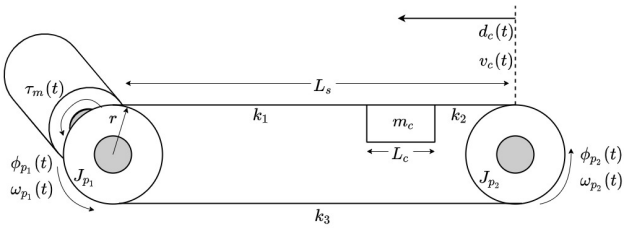

FIGURE 11. Schematic outlining a model of the belt-drive CoG compensation subsystem.

planar components by x_n^M, z_n^M and expanding $\left(\boldsymbol{p}_i\right)_n^M$ with constraint (a), we get

$$\begin{aligned} x_n^M(s) &= y_i(s) + \tan(\psi_S)\, x_i - \sec(\psi_S)\, \Delta p_y, \\ z_n^M(s) &= z_i(s) - \Delta p_z, \\ \Delta p_x &= \sec(\psi_S)\, x_i - \tan(\psi_S)\, \Delta p_y. \end{aligned} \tag{19}$$

Using the panel dimensions, Δp_y, Δp_z can be specified to aptly position the hexacopter, and the Δp_x is computed from (19). Body-frame end-effector locations can then be recovered from $x_n^M(s)$, $z_n^M(s)$. Along with the orientation $\psi_n = \alpha_S$, they used to command the $\boldsymbol{q}_a, \alpha_n$ using the previously developed inverse kinematics solution (10).

B. DYNAMICS

There are several approaches used to model aerial manipulator dynamics. One way is to add an additional forcing term to the hexacopter equations, which represents the reaction of the robot arm's motion at the hexacopter's CoG. This is done in works such as [34] and [72]. Alternatively, and this is the model we present here, the equations of motion can be derived from first principles using the Euler-Lagrange equations. References [69] and [70] extend the classical Euler-Lagrange formulation for robot manipulator dynamics, found in [73], to aerial manipulators. In this work, the slider dynamics are also included in the model.

Let the system Lagrangian be given by $\mathcal{L} = \mathcal{T} - \mathcal{V}$, where $\mathcal{T}$, $\mathcal{V}$ are the total kinetic and potential energies of the combined system. The kinetic energy of the moving components are due to the hexacopter, robot arms, end-effector, counterweight, and pulleys. The set $K_D = \{1, 2, 3, 4, n, c, B, p_1, p_2\}$ contains the subscripts which indicate the moving components. The kinetic and potential energy are given by

$$\begin{aligned} \mathcal{T} &= \sum_{k \in K_m} \frac{1}{2} m_k \left(\dot{\boldsymbol{p}}_k^E\right)^T \dot{\boldsymbol{p}}_k^E + \frac{1}{2} \left(\boldsymbol{\omega}_k^E\right)^T I_k^E \boldsymbol{\omega}_k^E \\ \mathcal{V} &= \sum_{k \in K} m_k g \boldsymbol{e}_3^T \boldsymbol{p}_k^E + \frac{1}{2} \left[\sum_{j=1}^{2} k_j \left(r_p \phi_{p_j} - d_c\right)^2 \right. \\ &\quad \left. + k_3 r_p^2 \left(\phi_{p_1} - \phi_{p_2}\right)^2 \right], \end{aligned} \tag{20}$$

where the k_j, ϕ_{p_j} are defined in a schematic of the slider in Fig. 11 that is based on drive-belt models [74]. The I_k^E are the inertia tensors defined with respect to $\mathcal{F}_E$, which can be decomposed into $I_k^E = R_B^E I_k \left(R_B^E\right)^T$, where I_k is the diagonal inertia tensor of component k defined with respect to the component's CoG position [73].

We define $K_M = \{1, 2, 3, 4, n\}$, $K_c = \{c, p_1, p_2\}$ to separate the manipulator and slider components. Defining $\boldsymbol{q}_c = \left(\phi_{p_1}\ \phi_{p_2}\ d_c\right)^T$ and noting that $\boldsymbol{p}_k^E = \boldsymbol{p}_B^E + R_B^E \boldsymbol{p}_k^B$ for $k \in K_m$, then, analogously to (13), for $i_1 \in K_M$, $i_2 \in K_c$, [69]

$$\begin{aligned} \dot{\boldsymbol{p}}_{i_1}^E &= \dot{\boldsymbol{p}}_B^E - S\left(R_B^E \boldsymbol{p}_{i_1}^B\right) T(\boldsymbol{\Theta}_B)\, \dot{\boldsymbol{\Theta}}_B + R_B^E J_{i_1,p} \dot{\boldsymbol{q}}_a, \\ \dot{\boldsymbol{p}}_{i_2}^E &= \dot{\boldsymbol{p}}_B^E - S\left(R_B^E \boldsymbol{p}_{i_2}^B\right) T(\boldsymbol{\Theta}_B)\, \dot{\boldsymbol{\Theta}}_B + R_B^E J_{i_2,p} \dot{\boldsymbol{q}}_c, \\ \boldsymbol{\omega}_{i_1}^E &= T(\boldsymbol{\Theta}_B)\, \dot{\boldsymbol{\Theta}}_B + R_B^E J_{i_1,\omega} \dot{\boldsymbol{q}}_a, \\ \boldsymbol{\omega}_{i_2}^E &= T(\boldsymbol{\Theta}_B)\, \dot{\boldsymbol{\Theta}}_B + R_B^E J_{i_2,\omega} \dot{\boldsymbol{q}}_c. \end{aligned} \tag{21}$$

The Jacobians $J_{i,p}$, $J_{i,\omega}$ are the linear and angular velocity Jacobians respectively, which can be appropriately defined for each component (Appendix). Further, $\boldsymbol{p}_k^B = \boldsymbol{p}_M^B + \bar{\boldsymbol{p}}_k$ for all $k \in K_m$, where the $\bar{\boldsymbol{p}}_i$ are the positions expressed in the manipulator frame $\mathcal{F}_M$ as defined in Section III-A.

Let $\boldsymbol{X} = \left(\boldsymbol{p}_B^{E^T}\ \boldsymbol{\Theta}_B\ \boldsymbol{q}_a\ \boldsymbol{q}_c\right)^T \in \mathbb{R}^{11}$ be the combined system's state vector. By substituting (21) into $\mathcal{T}$ from (20) and rearranging, we can write $\mathcal{T} = \frac{1}{2} \boldsymbol{X}^T D \boldsymbol{X}$, where D is the symmetric, positive-definite inertia matrix [73]. Defining the belt stiffness matrix κ as

$$\kappa_c = \begin{pmatrix} (k_1 + k_3) r_p^2 & -k_3 r_p^2 & -k_1 r_p \\ -k_3 r_p^2 & (k_2 + k_3) r_p^2 & -k_2 r_p \\ -k_1 r_p & -k_2 r_p & k_1 + k_2 \end{pmatrix},$$

$$\kappa = \begin{pmatrix} \boldsymbol{0}_8 & \boldsymbol{0}_{8\times 3} \\ \boldsymbol{0}_{3\times 8} & \kappa_c \end{pmatrix},$$

and $\boldsymbol{g}(\boldsymbol{X}) = \frac{\partial \mathcal{V}_g}{\partial \boldsymbol{X}}$, where $\mathcal{V}_g$ is the gravitational potential energy from $\mathcal{V}$, the Euler-Lagrange equations yield

$$D(\boldsymbol{X})\, \ddot{\boldsymbol{X}} + \boldsymbol{c}\left(\boldsymbol{X}, \dot{\boldsymbol{X}}\right) + \boldsymbol{g}(\boldsymbol{X}) + \kappa \boldsymbol{X} + \dot{B} \boldsymbol{X} = \boldsymbol{\tau}_{BM}.$$

Here, B is a diagonal matrix representing a lumped viscous damping model. $\boldsymbol{c}(\boldsymbol{X}, \dot{\boldsymbol{X}})$ contain the Coriolis and centrifugal terms and the $\boldsymbol{c}_i$ are given by the Christoffel symbols [73]

$$\begin{aligned} \boldsymbol{c}_i\left(\boldsymbol{X}, \dot{\boldsymbol{X}}\right) &= \dot{\boldsymbol{X}}^T C_i(\boldsymbol{X})\, \dot{\boldsymbol{X}}, \\ C_i(\boldsymbol{X}) &= \frac{1}{2} \left[\frac{\partial D_i}{\partial \boldsymbol{X}} + \left(\frac{\partial D_i}{\partial \boldsymbol{X}}\right)^T - \frac{\partial D}{\partial \boldsymbol{X}_i} \right], \end{aligned}$$

where D_i is the ith column of the inertia matrix.

A special case of the above can be obtained after making certain simplifications. If we consider the manipulator and CoG compensation subsystems to be fixed to a testing frame by a hook instead of being attached to a moving drone, we can drop the translation equations for $\boldsymbol{p}_B^E$ and keep only the pitch equation θ, along with the $\boldsymbol{q}_a$, $\boldsymbol{q}_c$. This is equivalent to a hovering condition of the aerial manipulator, where the rotors are in charge of maintaining the position. Furthermore, if we neglect the stretching of the belts, we have that

$d_c = r_p\phi_{p_1} = r_p\phi_{p_2}$, so that $\boldsymbol{q}_c = d_c$, and the applied forces only act at the manipulator joints and counterweight platform.

In light of these simplifications, the equations describing θ and d_c are

$$\begin{aligned} J_{yy}\ddot{\theta} &+ \left[-m_c\left(\boldsymbol{p}_c^B\right)_z + \frac{I_{p_y}}{r_p}\right]\ddot{d}_c + \sum_{k\in K_M} m_k\left(R_0\boldsymbol{p}_k^B\right)^T J_{k,p}\ddot{\boldsymbol{q}}_a \\ &+ 2\sum_{k\in K_M} m_k\left(\boldsymbol{p}_k^B\right)^T J_{k,p}\dot{\boldsymbol{q}}_a\dot{\theta} + 2m_c\left(\boldsymbol{p}_c^B\right)^T J_{c,p}\dot{d}_c\dot{\theta} \\ &+ \sum_{k\in K_M} m_k\left[\left(R_0\boldsymbol{p}_k^B\right)^T\frac{\partial J_{k,p}}{\partial \boldsymbol{q}_a}\dot{\boldsymbol{q}}_a + \dot{\boldsymbol{q}}_a^T\left(R_0J_{k,p}\right)^T J_{k,p}\right]\dot{\boldsymbol{q}}_a \\ &+ \sum_{k\in K} m_k g\boldsymbol{p}_k^{B^T}\begin{pmatrix} c_\theta \\ 0 \\ s_\theta\end{pmatrix} = 0, \end{aligned} \tag{22}$$

$$\begin{aligned} &\left[-m_c\left(\boldsymbol{p}_c^B\right)_z r_p + I_{p_y}\right]\ddot{\theta} + \frac{1}{r_p}\left(m_c r_p^2\right. \\ &\left.+I_{p_y}\right)\ddot{d}_c + m_c r_p\left(\boldsymbol{p}_c^B\right)_x\dot{\theta}^2 + b_c r_p\dot{d}_c + m_c g h_c\sin\theta \\ &= \tau_m(t), \end{aligned} \tag{23}$$

where

$$J_{yy} = \sum_{k\in K_M} I_{k,y} + m_k\left\|\boldsymbol{p}_k^B\right\|^2,\ R_0 = R_Y\left(\frac{\pi}{2}\right),$$
$$\frac{\partial J_{k,p}}{\partial \boldsymbol{q}_a}\dot{\boldsymbol{q}}_a = \frac{\partial J_{k,p}}{\partial q_1}\dot{q}_1 + \frac{\partial J_{k,p}}{\partial q_2}\dot{q}_2,$$

the $I_{k,y}$ is the y-component of I_k, and b_c is the viscous damping acting on the slider. The J_{yy} term represents the total moment of inertia with respect to the y-axis of the base's, or hexacopter's, CoG.

It is possible to rewrite some terms in the first equation using the Jacobians $J_{\boldsymbol{q}_a}^{\bar{p}}$, $J_{d_c}^{\bar{p}}$ from (12), which better shows the inclusion of the velocity of the CoG in addition to the position of the CoG resulting from the gravity terms. This allows it to be treated as a disturbance that can be compensated for in the robust control scheme proposed in [75].

The DC motor torque $\tau_m(t) = K_t i_m(t)$, where $i_m(t)$ is the supplied current. The DC motor equation for i_m is [76]

$$L_m\frac{di_m}{dt} = -R_m i_m - K_e\frac{d_c}{r_p} + V_m(t),$$

where L_m, R_m, K_e, K_t, V_m are the motor inductance, resistance, velocity and torque constants, and applied voltage, respectively.

V. CONTROL SYSTEM

Fig. 12 shows a block diagram of the proposed control system.

In the motion planning phase, the inverse kinematics are used to compute the reference joint angles $q_{1,d}, q_{2,d}$ using the desired end-effector positions from (19). The manipulator joints with imposed trajectory function $\boldsymbol{q_a} = \boldsymbol{q_a}(\mathbf{t})$ can be set and tracked with the internal servo motor controllers. Then

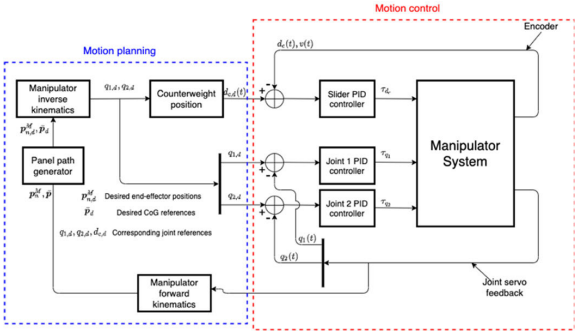

FIGURE 12. Proposed control system consisting of motion planning using an appropriate choice of slider control law to counterbalance the CoG shift, and separate motion controllers for each actuator.

we can rewrite the corresponding terms, which are known functions of time, as

$$\begin{aligned} Q_1(t) &= \sum\nolimits_{k\in K_M} m_k\left(R_0\boldsymbol{p}_k^B\right)^T J_{k,p}\ddot{\boldsymbol{q}}_a \\ &+ \sum\nolimits_{k\in K_M} m_k\left[\left(R_0\boldsymbol{p}_k^B\right)^T\frac{\partial J_{k,p}}{\partial \boldsymbol{q}_a}\dot{\boldsymbol{q}}_a + \dot{\boldsymbol{q}}_a^T\left(R_0J_{k,p}\right)^T J_{k,p}\right]\dot{\boldsymbol{q}}_a, \\ Q_2(t) &= 2\sum\nolimits_{k\in K_M} m_k\left(\boldsymbol{p}_k^B\right)^T J_{k,p}\dot{\boldsymbol{q}}_a. \end{aligned}$$

Next, we obtain the τ_m required to move the slider at constant velocity, i.e. $\ddot{d}_c = 0$. First, we rewrite (22) and (23) and decouple $\ddot{\theta}, \ddot{d}_c$ as follows:

$$\begin{pmatrix} J_{yy} & b \\ br_p & d\end{pmatrix}\begin{pmatrix}\ddot{\theta}\\ \ddot{d}_c\end{pmatrix} = -\begin{pmatrix} f_1\left(t,\ \theta, d_c, \dot{\theta},\ \dot{d}_c\right) \\ f_2\left(t,\ \theta,\ d_c, \dot{\theta}, \dot{d}_c\right) + \tau_m(t)\end{pmatrix},$$
$$\begin{pmatrix}\ddot{\theta}\\ \ddot{d}_c\end{pmatrix} = -\frac{1}{J_{yy}d - b^2r_p}\begin{pmatrix} df_1 - bf_2 - b\tau_m \\ -br_pf_1 + J_{yy}f_2 + J_{yy}\tau_m\end{pmatrix}.$$

Setting $\ddot{d}_c = 0$ requires $\tau_m = \frac{b}{J_{yy}}r_pf_1 - f_2$, which can be substituted into the equation for $\ddot{\theta}$

$\ddot{\theta} = -\frac{1}{J_{yy}d - b^2r_p}\left(df_1 - bf_2 - \frac{b^2}{J_{yy}}r_pf_1 + bf_2\right) = -\frac{f_1}{J_{yy}}$. This is just (22) with $\ddot{d}_c = 0$, $\dot{d}_c = v_c$. Noting that $\left(\boldsymbol{p}_c^B\right)^T J_{c,p} = -\left(\boldsymbol{p}_c^B\right)_x$, (22) can now be written as

$$\begin{aligned} J_{yy}\ddot{\theta} - 2m_c\left(\boldsymbol{p}_c^B\right)_x v_c\dot{\theta} + \sum_{k\in K} m_k g\boldsymbol{p}_k^{B^T}\begin{pmatrix} c_\theta \\ 0 \\ s_\theta\end{pmatrix} \\ + Q_2(t)\dot{\theta} + Q_1(t) = 0. \end{aligned} \tag{24}$$

Recall that $\left(\boldsymbol{p}_c^B\right)_x = -d_c + R_1c_{\phi_1} + p_{M\,x}^B$. Then, choosing $x_1 = \theta$, $x_2 = \dot{\theta}$, we have

$$\begin{aligned} \dot{x}_1 &= x_2 \\ \dot{x}_2 &= \frac{-1}{J_{yy}}\left[\sum_{k\in K} m_k g\left(p_{k\,z}^B s_\theta\right) + \sum_{k\in K^*} m_k g\left(p_{k\,x}^B c_\theta\right)\right] \\ &\quad - \frac{m_c}{J_{yy}}\left(gc_\theta - 2v_c\dot{\theta}\right)\left(p_{M\,x}^B + R_1c_{\phi_1}\right) \\ &\quad + \frac{m_c}{J_{yy}}\left(gc_\theta - 2v_c\dot{\theta}\right)d_{c,d} - \frac{Q_1(t) + Q_2(t)\dot{\theta}}{J_{yy}}, \end{aligned}$$

which is of the form $\dot{\boldsymbol{x}} = \boldsymbol{f}(t, \boldsymbol{x}) + \boldsymbol{g}(\boldsymbol{x})\, u$ for $u = d_c, d$, $\boldsymbol{x} = \begin{pmatrix} x_1 \\ x_2 \end{pmatrix}$. A feedback linearization control law can be chosen as [77]

$$u = p^B_{Mx} + \frac{p^B_{c\,z} g s_\theta}{g c_\theta - 2 v_c \dot{\theta}} + R_1 c_{\phi_1} + \frac{1}{m_c \left(g c_\theta - 2 v_c \dot{\theta}\right)} \left[v + \sum_{k \in K^*} m_k \left(\boldsymbol{p}^B_k\right)^T \begin{pmatrix} c_\theta \\ 0 \\ s_\theta \end{pmatrix} + Q_1(t) + Q_2(t)\, \dot{\theta} \right]. \tag{25}$$

We refer to the control law in (25) as the as the *dynamic control law*. The state space model under the control law (25) is reduced to the double integrator

$$\begin{pmatrix} \dot{x}_1 \\ \dot{x}_2 \end{pmatrix} = \begin{pmatrix} 0 & 1 \\ 0 & 0 \end{pmatrix} \begin{pmatrix} x_1 \\ x_2 \end{pmatrix} + \begin{pmatrix} 0 \\ 1 \end{pmatrix} v,$$

which has a full-rank controllability matrix $C = \begin{pmatrix} B & AB \end{pmatrix} = \begin{pmatrix} 0 & 1 \\ 1 & 0 \end{pmatrix}$, implying the system is also stabilizable. A PID controller of the form

$$v = -\begin{pmatrix} \mu_1^2 & \mu_2^2 & -(\mu_1 \mu_2)^2 + \mu_3^2 \end{pmatrix} \begin{pmatrix} \boldsymbol{x} \\ x_3 \end{pmatrix}$$

can be chosen to stabilize the system and track $\theta_d = 0$ for some $\mu_1, \mu_2, \mu_3 \in \mathbb{R}$ and $x_3 = \int_0^t -\theta(\tau)\, d\tau$. The characteristic equation under this control is

$$s^3 + \mu_2^2 s^2 + \mu_1^2 s + \left(\mu_3^2 - \mu_1^2 \mu_2^2\right) = 0. \tag{26}$$

All the poles of (26) are in the left half-plane.

We emphasize that the dynamic control law is equivalent to the static control law obtained by solving (2) when $\theta = 0$. In a dynamic setting in which $\ddot{d}_c \neq 0$ and θ is larger, the coupled dynamics can be used with $u = \tau_m$. Although this is beyond the scope of the paper. A stabilizing control law can be derived in that setting.

To demonstrate the efficacy of the mechanism in the current setting, a slider motion controller in the form of a discrete-time PID controller is used to send the counterweight to a precomputed slider position, $d_{c,d}$. The motion controllers for the manipulator joint angles are embedded into the servo motors and can accurately reach the commanded angles q_1, q_2.

We use the Raspberry Pi (RPi) to implement the motion controllers. Fig. 6 contains the schematic used to realize the control system on the test bench. The joint angle values $\boldsymbol{q}_{a,d} = \left(q_{1,d}, q_{2,d}\right)^T$ are internally computed using inverse kinematics for some given end-effector positions. The $\boldsymbol{p}_k$ are known from the fixed structure and the moving links from the computed $\boldsymbol{q}_{a,d}$. The slider setpoint $d_{c,d}$ is then internally computed using (25) with $\theta = 0$.

After computing the required setpoints as outlined in Fig. 12, the corresponding PWM is output from the RPi to each joint servo motor, which uses its internal motion controller to send the joint angles to $\boldsymbol{q}_{a,d}$. A discrete-time PID controller is implemented using the RPi by using slider position encoder values to update the control signal u_c used to drive the DC motor speed. This is done one sample at a time using the following discrete PID law:

$$u_c[k] = k_p\left(e_c[k]\right) + k_d\left(e_c[k] - e_c[k-1]\right) + k_i \sum_{j=0}^{k} e_c[j],$$

$$e_c[k] = d_{c,d} - d_c[k].$$

Here, $u[k]$ is the control signal value at time $k\Delta T$, where ΔT is the sampling time. The sampling time is restricted by the encoder resolution. The operation continues until the error is reasonably close to zero. The RPi is also interfaced with the IMU and logs the tilt angle data $\theta[k]$. In a dynamic setting with high tilt angle values, θ can be used to update the dynamic law (25) and generate a new slider setpoint.

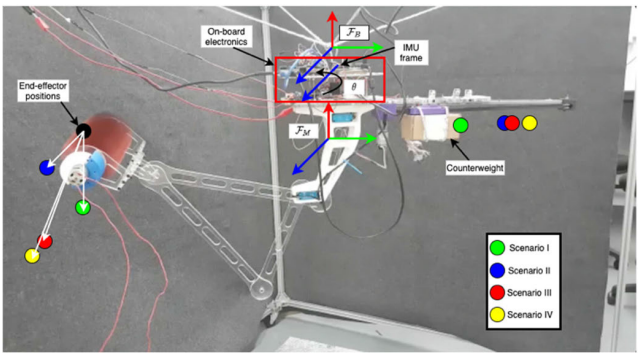

FIGURE 13. Proposed manipulator with CoG compensation system, showing end-effector and slider positions set for each experiment.

VI. EXPERIMENT

A. EXPERIMENTAL SETUP

The objective of the conducted experiment is to quantify the effectiveness of the proposed CoG compensation mechanism by compensating the system's shift in tilt angle during operation. Fig. 13 shows the experimental setup in an initial, stable configuration. The system was hook-fixed to a rigid cable system to simulate the stable hovering of a hexacopter and demonstrate a proof of concept. The 100 g counterweight represents a battery during aerial manipulation. The IMU is fixed beneath the base frame $\mathcal{F}_B$ with the same orientation. The total mass of the platform and interfaced components is about 1.29 kg, reported in Table 2. This is well below a typical hexacopter maximum payload, which renders the system feasible for deployment on solar panels.

Step inputs to the system are provided in the form of fixed values for the manipulator joint angle $\boldsymbol{q}_a$. Four different scenarios, each in which the joint angles are changed from an initial to final configuration, are conducted in the experiments. The values of the end-effector positions are chosen so that the slider position will be commanded to a different position in each scenario. When deployed on a solar panel,

TABLE 3. Joint angle, slider, and end-effector positions for each scenario.

Scenario	$\boldsymbol{q}_{a,f}$ (deg)	$\Delta\boldsymbol{q}_{a,f}$ (deg)	$d_{c,ss}$ (cm)	$\boldsymbol{p}_n^M$, $\|\boldsymbol{p}_n^M\|$ (cm)
I	(109, 96)	(4, -19)	13.00	(41.17, -12.13), 42.92
II	(118, 117)	(13, 2)	17.50	(47.83, 0.79), 47.84
III	(123, 96)	(18, -19)	18.60	(54.86, -20.01), 58.40
IV	(139, 96)	(24, -19)	21.50	(56.33, -24.83), 61.56

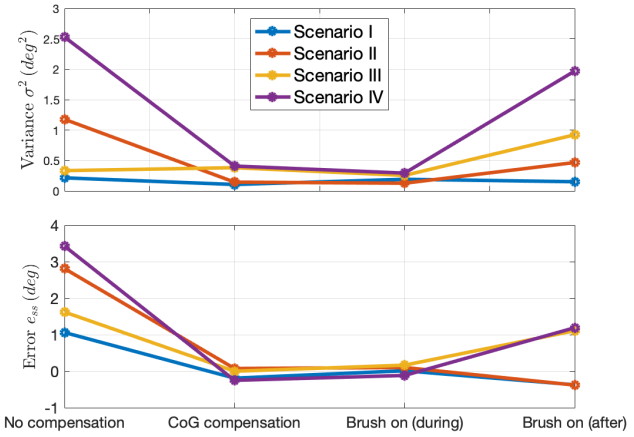

FIGURE 14. Variance and steady-state error values across all scenarios.

the path-planning formulation of Section IV-A4 can be used to determine the end-effector positions instead.

The joint angles $\boldsymbol{q}_{a,i}$ for the initial equilibrium configuration are equal for each scenario at (105, 115) degrees, with the brush located at $\boldsymbol{p}_n^M = (45.05,\ 5.37)$ cm, $\|\boldsymbol{p}_n^M\| = 33.94$ cm, and slider position $d_c = 7.5$ cm. The final joint angles, end-effector positions, and steady-state slider locations for each scenario are given in Table 3. We note that the end-effector load torque acting on the system is due to the horizontal component of $\boldsymbol{p}_n^M$ when the tipping angle $\theta = 0$. However, as indicated by the $\|\bar{\boldsymbol{p}}\|$ term in the system dynamics, readily shown by linearizing (24), both horizontal and vertical components will contribute when $\theta \neq 0$. Both joint velocity values are equal and constant across all scenarios.

B. RESULTS

To quantify the results of each Scenario, the tipping angle was measured in the following four conditions:

1) No CoG compensation (Off-Uncompensated),
2) With CoG compensation (Off-Compensated),
3) Brush on with CoG compensation during joint motion, (On-During), and
4) Brush on with CoG compensation after joint motion (On-After).

From here onwards, the names in parentheses will be used to denote the condition of a particular experiment. Off-Uncompensated and Off-Compensated refer to experiments with the brush turned off and respectively with and without CoG compensation. The latter two refer to experiments with CoG compensation and with the brush turned on.

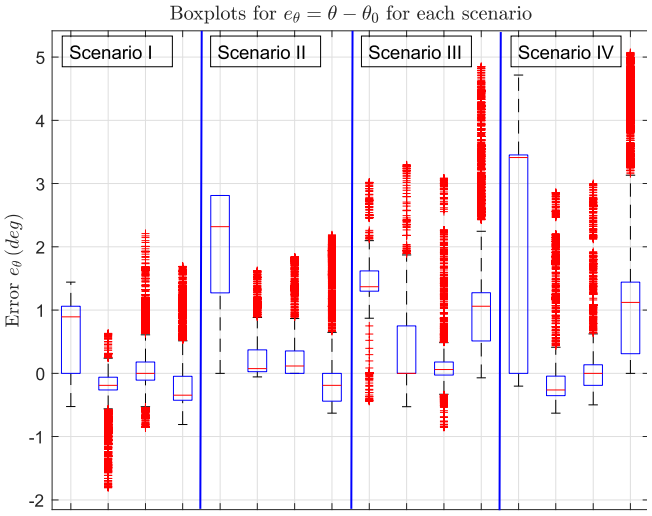

FIGURE 15. Variation of e_θ for each Scenario, in the following order (left to right): Off-Uncompensated, Off-Compensated, On-During, and On-After.

On-During means the robot undergoes CoG compensation and joint motion simultaneously, while On-After means the CoG compensation is done shortly after the joint motion is complete.

The tipping angle θ was measured and stored using the IMU. We define the error to be $e_\theta[k] = \theta[k] - \theta_0$, the steady-state error by $e_{ss} = e[N]$, the mean by $\mu = \frac{1}{N}\sum_{i=0}^{N}\theta(i)$, and the variance by $\sigma^2 = \frac{1}{N}\sum_{i=0}^{N}(\theta[i]-\mu)^2$, where N is the total number of samples.

We found that each metric is indicative of performance. The steady-state error demonstrates the effectiveness of the slider mechanism at minimizing the tipping caused by the joint motion, while the variance helps characterize the transient response in that higher variance values imply more vibratory behavior. The mean value is reported to help understand the range of angle values in that particular experiment. The error and variance across each case are plotted in Fig. 14. Boxplots of the error e_θ for each Scenario and condition are shown in Fig. 15 to visually compare the distributions in each set of readings, with the conditions ordered left to right as Off-Uncompensated, Off-Compensated, On-During, and On-After.

In all cases, the uncompensated system results in steady-state and mean errors further away from zero than the ones with compensation. The steady-state error values improve notably upon adding the compensation system as the tipping angle is nearly zeroed. The error is minimized when the brush is off, since the slider was positioned without accounting for the disturbance caused by the brush.

Between the two configurations in which the brush is turned on, the On-During condition shows improved stabilization both in terms of variance and error. Both steady-state and mean errors are nearly zero across all Scenarios in the On-During condition, while On-After results in some offset in the same metrics, as well as higher variance. These results

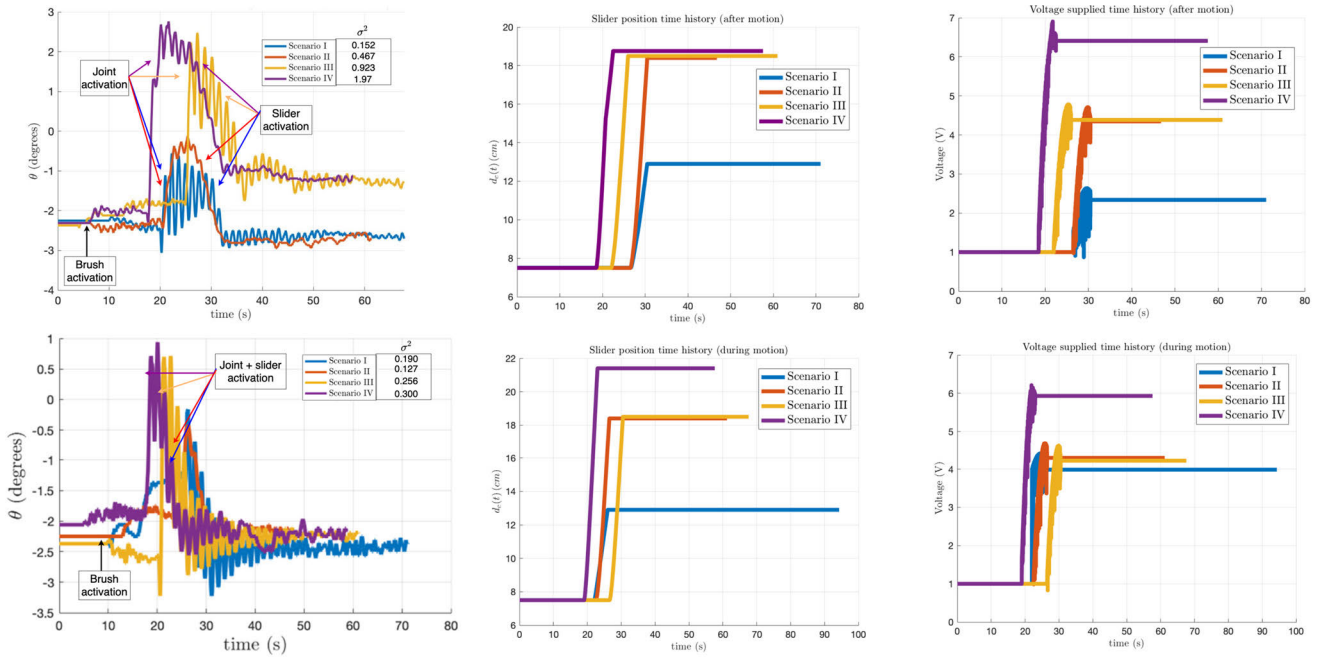

FIGURE 16. Plots of the brush on, compensated after motion (above) and during motion (below), with slider position (middle) and control.

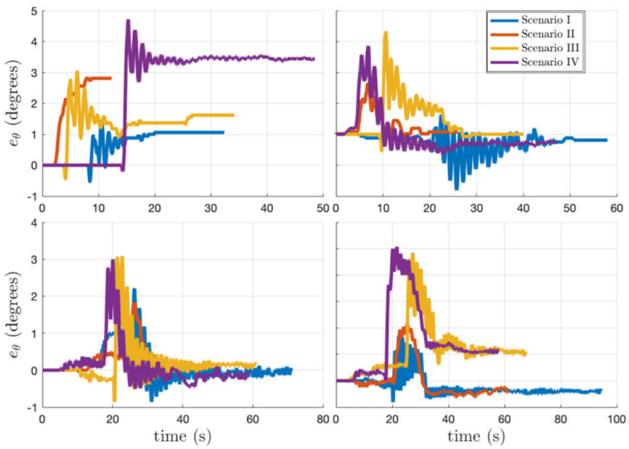

FIGURE 17. Tipping angle error time history. Top: Off-Uncompensated and Off-Compensated, bottom: On-During and On-After.

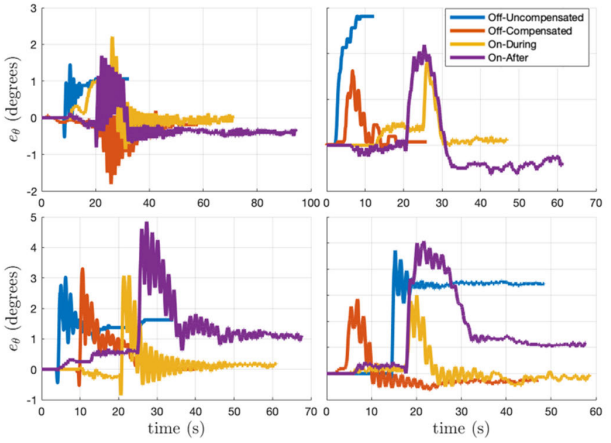

FIGURE 18. Plots of tipping angle error vs. time for Scenarios I-II (top) and III-IV (bottom), left to right, under each configuration.

show that effectively compensating the CoG can also reduce the disturbance induced by the brush. Therefore, On-During is the recommended mode of operation when the brush is on.

In two out of the four configurations for each scenario, the brush was turned on to simulate the operating behavior of the cleaning system and to confirm CoG compensation with an active brush.

Fig. 16 shows the time history of the tipping angle, as well as the slider position and the DC motor voltage input as determined by the PID controller. The tipping angle error is also presented in Fig. 17 to illustrate the tipping angle deviations in each case. Fig. 18 shows the same but with subfigures separated by scenario rather than mode of operation.

The values of the local CoG positions are also computed using the trajectories of the slider, joints, end-effector, and (1). For comparison, the local CoG position trajectory was computed under the same configuration but without the presence of the slider compensating system. The time histories for each are displayed in Fig. 19 and Fig. 20, and the final values of $\overline{p}_x$ in the robot plane in Fig. 21.

To scale the results, reference lengths $L_x^* = -R_1 c_{\phi_1} + L_1 + L_3 = 58.5\ cm$ and $L_z^* = -R_1 s_{\phi_1} + L_1 + L_3 = 59.2\ cm$ are chosen to nondimensionalize the CoG position values by $\tilde{p_x} = \frac{\overline{p}_x}{L_x^*}$, $\tilde{p_z} = \frac{\overline{p}_z}{L_z^*}$.

In Fig. 19, when the slider compensating system is removed, system's mass is concentrated ahead of the hook's

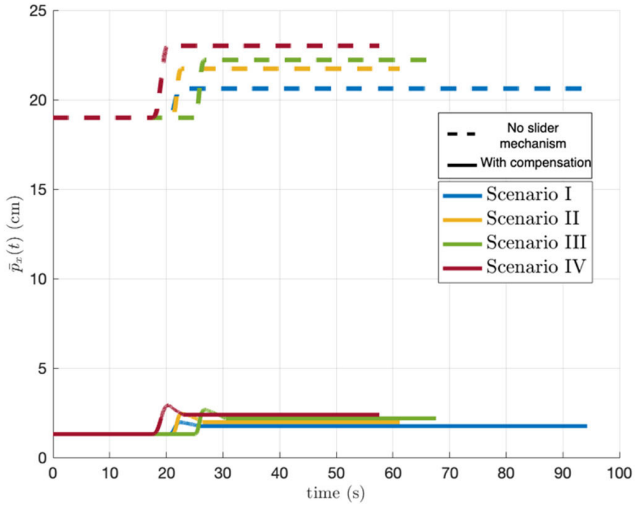

FIGURE 19. Horizontal CoG position trajectory for each scenario, comparing experiment with simulation without slider. Configuration: On-During.

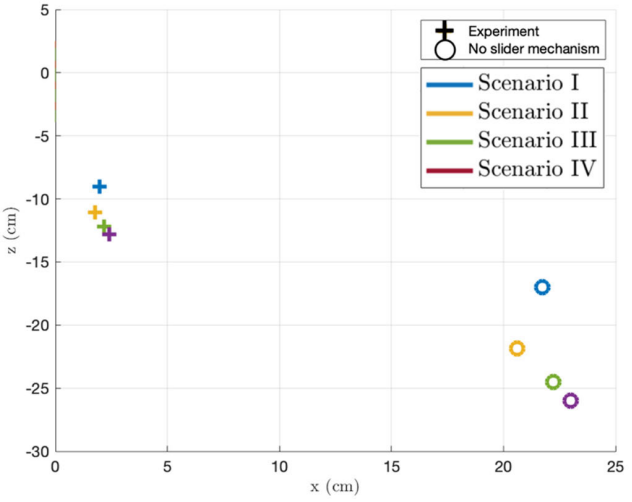

FIGURE 21. Final CoG position values in the Cartesian plane, comparing experiment with simulation without slider. Configuration: On-During.

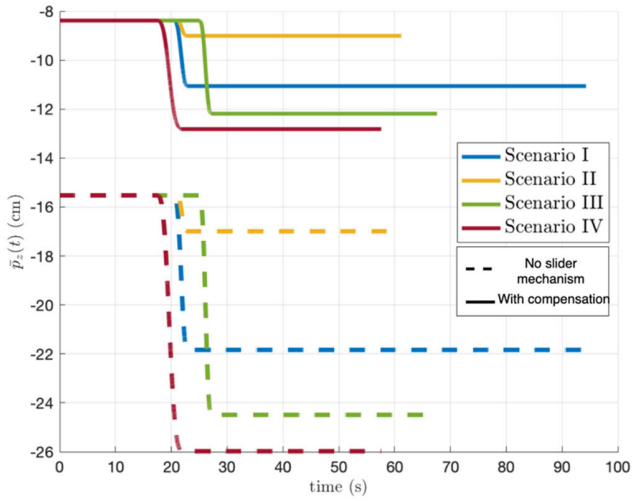

FIGURE 20. Vertical CoG position trajectory for each scenario, comparing experiment with simulation without slider. Configuration: On-During.

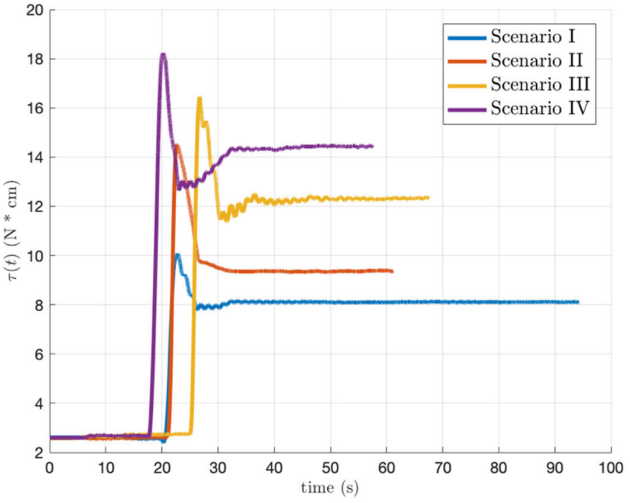

FIGURE 22. Gravitational torque (effective at the hook) acting on the robot. Configuration: On-During.

CoG position. This is why the $\overline{p}_x$ values are much larger than with the presence of the slider. In addition to this difference, the *shift* in CoG resulting from the joint motion is also lower when the slider is present (a maximum of $\Delta\tilde{p_x} = 2.05\%$) than without (a maximum of $\Delta\tilde{p_x} = 6.84\,\%$). In addition to the horizontal CoG variation, the norm of the CoG vector in Fig. 21 encodes the variation of the vertical component.

In the robot plane in Fig. 21, the same steady-state CoG position values with compensation are much closer to the origin with an average $\tilde{p_x} = 3.93\%$, while those with no CoG compensation system average at $\tilde{p_x} = 38.5\%$. This difference in CoG shift will significantly destabilize the system by increasing the induced gravitational torque and, subsequently, the tilt angle. In hexacopter applications, this will result in a higher power requirement from the rotor motors for stabilization, and may even fail at doing so. To put this into perspective, moving the counterweight (with compensation experiments) resulted in $\tilde{p_x} = 3.93\%$, while fixing its position at the beginning of the slider (no compensation experiment) resulted in $\tilde{p_x} = 4.79\%$. This CoG difference of 0.85% reduced the tilt angle by 1^{o}-3^{o} (Fig. 19) depending on the experimental scenario. Based on this, it is reasonable to assume simulated value of $\tilde{p_x} = 38.5\%$ will yield much higher values.

When the value of θ is not small, both $\overline{p}_x$ and $\overline{p}_z$ contribute to the torque induced by gravity on the system. This is represented by the gravity term in (22) and (24), which can be rewritten as $m_T g \left(\overline{p}_x^B c_\theta + \overline{p}_z^B s_\theta\right)$. Applying the definition of the gravitational torque

$$\tau = R_Y(\theta)\, S\left(\overline{\boldsymbol{p}}_{BM}^B\right) \boldsymbol{g}$$

yields the same term about the y-axis. The time history of the gravitational torque causing the rotation for each case is shown in Fig. 22.

VII. CONCLUSION

In this work, an aerial manipulator system with a five-bar parallel robot and bendable end-effector was proposed for the purpose of solar panel cleaning operation. The primary advantage of the system is in its design to reduce the load torque and the presence of a slider-battery system to compensate for shifts in the CoG position. This allows significant forward reach of the end-effector with minimal shifts in the CoG position, which was shown in an analysis of the robot workspace subject to practical physical constraints.

Several experiments were conducted on the aerial manipulator fixed to a testing setup. An end-effector with brush was moved to simulate the cleaning operation, and the slider mechanism was used to compensate for the shift in the CoG location. The readings on the tilt angle indicate that it is best to move the counterweight during the joint motion, and that the counterweight can significantly affect the tilting of the system as well reduce the transient oscillations during motion. A 34.5% difference in the horizontal CoG shift is computed between the compensated system and the same system without the mechanism present. Hence, the compensation substantially improves the stability of the system by decreasing the tilt angle and reduces the constant stabilizing power required by the hexacopter during cleaning. The experiments also show that CoG compensation while moving the joints reduces the overall tilt angle vibrations.

The advantages of the proposed system are threefold: to provide a robust CoG position compensation system that improves stability during cleaning, to minimize the payload by optimizing the structural geometry, and to utilize the parallel robot design to reduce the torque on the joint servo motors while maintaining the required workspace.

Finally, a path planning scheme for solar panel cleaning operation was presented based on the exact kinematics of the system. The solution can be used to autonomously generate paths, which then require a motion controller for execution. The dynamics of the combined system were given based on previously developed work [69], [70], [73]. A modification was made to also include the slider motion, and a reduced fourth-order model coupling the tilt angle and slider position was derived under hovering operation with simple inputs. Feedback linearization was applied to the coupled system to obtain a dynamic control law. It was shown that the dynamic control law is equivalent to the static control law obtained using CoG balancing when the tilt angle is zero.

ACKNOWLEDGMENT

This article represents the opinions of the author(s) and does not mean to represent the position or opinions of the American University of Sharjah.

APPENDIX

The Jacobian relating the passive joint angles $\boldsymbol{q}_p = \begin{pmatrix} q_3 & q_4 \end{pmatrix}^T$ to the active joint angles $\boldsymbol{q}_a = \begin{pmatrix} q_1 & q_2 \end{pmatrix}^T$ is given by

$$J_{q_a}^{q_p} = \frac{1}{L_3 L_4 s_{3,4}} \begin{pmatrix} -L_1 L_4 s_{1,4} & L_2 L_4 s_{2,4} \\ -L_1 L_3 s_{1,3} & L_2 L_3 s_{2,3} \end{pmatrix}.$$

The Jacobians $J_{i,p}$, $J_{i,\omega}$, defined in Section IV-B, relate the linear and angular velocity respectively of the component indicated by i to the actuation variables $\dot{\boldsymbol{q}}_a$,$\dot{\boldsymbol{q}}_c$. The Jacobians are deduced from the robot kinematics. The linear velocity Jacobians are

$$J_{1,p} = \frac{L_1}{2} \begin{pmatrix} -s_1 & 0 \\ 0 & 0 \\ c_1 & 0 \end{pmatrix}, \; J_{2,p} = \frac{L_2}{2} \begin{pmatrix} 0 & -s_2 \\ 0 & 0 \\ 0 & c_2 \end{pmatrix},$$

$$J_{3,p} = L_1 \begin{pmatrix} -s_1 & 0 \\ 0 & 0 \\ c_1 & 0 \end{pmatrix} + \frac{L_3}{2} \begin{pmatrix} -s_3 & 0 \\ 0 & 0 \\ c_3 & 0 \end{pmatrix} J_{q_a}^{q_p}$$

$$= \frac{1}{2 s_{3,4}} \begin{pmatrix} -L_1 \left(s_1 s_{3,4} - s_4 s_{1,3} \right) & -L_2 s_3 s_{2,4} \\ 0 & 0 \\ L_1 \left(c_1 s_{3,4} - c_4 s_{1,3} \right) & L_2 c_3 s_{2,4} \end{pmatrix},$$

$$J_{4,p} = L_2 \begin{pmatrix} 0 & -s_2 \\ 0 & 0 \\ 0 & c_2 \end{pmatrix} + \frac{L_4}{2} \begin{pmatrix} 0 & -s_4 \\ 0 & 0 \\ 0 & c_4 \end{pmatrix} J_{q_a}^{q_p}$$

$$= \frac{1}{2 s_{3,4}} \begin{pmatrix} L_1 s_4 s_{1,3} & -L_2 \left(s_2 s_{3,4} + s_3 s_{2,4} \right) \\ 0 & 0 \\ -L_1 c_4 s_{1,3} & L_2 \left(c_2 s_{3,4} + c_3 s_{24} \right) \end{pmatrix},$$

$$J_{n,p} = \frac{1}{s_{3,4}} \begin{pmatrix} L_1 s_4 s_{1,3} & -L_2 s_3 s_{2,4} \\ 0 & 0 \\ -L_1 c_4 s_{1,3} & L_2 c_3 s_{2,4} \end{pmatrix}, \; J_{c,p} = \begin{pmatrix} -1 & 0 & 0 \\ 0 & 0 & 0 \\ 0 & 0 & 0 \end{pmatrix}.$$

The angular velocity Jacobians are

$$J_{1,\omega} = \begin{pmatrix} 1 & 0 \end{pmatrix}, \; J_{2,\omega} = \begin{pmatrix} 0 & 1 \end{pmatrix},$$

$$J_{3,\omega} = \begin{pmatrix} 1 & 0 \end{pmatrix}, \; J_{q_a}^{q_p} = \frac{1}{L_3 s_{3,4}} \begin{pmatrix} -L_1 s_{1,4} & L_2 s_{2,4} \end{pmatrix},$$

$$J_{4,\omega} = \begin{pmatrix} 0 & 1 \end{pmatrix}, \; J_{q_a}^{q_p} = \frac{1}{L_4 s_{3,4}} \begin{pmatrix} -L_1 s_{1,3} & L_2 s_{2,3} \end{pmatrix},$$

$$J_{n,\omega} = J_{4,\omega}, \; J_{p_1,\omega} = \begin{pmatrix} 0 & 1 & 0 \end{pmatrix}, \; J_{p_2,\omega} = \begin{pmatrix} 0 & 0 & 1 \end{pmatrix}.$$

REFERENCES

[1] C. Nagori, "Unmanned aerial manipulators in construction—Opportunities and challenges," M.S. thesis, Civil Environ. Eng., Virginia Polytech. Inst. State Univ., Blacksburg, VA, USA, 2020.
[2] B. Chu, D. Kim, and D. Hong, "Robotic automation technologies in construction: A review," *Int. J. Precis. Eng. Manuf.*, vol. 9, no. 3, pp. 85–91, Jul. 2008.
[3] S. Siebert and J. Teizer, "Mobile 3D mapping for surveying earthwork projects using an unmanned aerial vehicle (UAV) system," *Autom. Construct.*, vol. 41, pp. 1–14, May 2014.
[4] K. Rawat and E. Lawrence, "A mini-UAV VTOL platform for surveying applications," *IAES Int. J. Robot. Autom.*, vol. 3, no. 4, pp. 259–267, Dec. 2014.
[5] F. Augugliaro, A. Mirjan, F. Gramazio, M. Kohler, and R. D'Andrea, "Building tensile structures with flying machines," in *Proc. IEEE/RSJ Int. Conf. Intell. Robots Syst.*, Nov. 2013, pp. 3487–3492.
[6] H. B. Khamseh, F. Janabi-Sharifi, and A. Abdessameud, "Aerial manipulation—A literature survey," *Robot. Auton. Syst.*, vol. 107, pp. 221–235, Sep. 2018.

[7] J. M. D. Delgado, L. Oyedele, A. Ajayi, L. Akanbi, O. Akinade, M. Bilal, and H. Owolabi, "Robotics and automated systems in construction: Understanding industry-specific challenges for adoption," *J. Building Eng.*, vol. 26, Nov. 2019, Art. no. 100868.

[8] M. A. K. Jaradat, S. M. Ashour, A. A. Matalkh, M. M. Elayyan, and A. M. Hammadneh, "Biologically inspired design of a glass climbing robot for remote services," *Int. J. Robot. Autom.*, vol. 25, no. 2, p. 132, 2010.

[9] T. Sorndach, N. Pudchuen, and P. Srisungsitthisunti, "Rooftop solar panel cleaning robot using omni wheels," in *Proc. 2nd Int. Conf. Eng. Innov. (ICEI)*, Jul. 2018, pp. 7–12.

[10] M. U. Hassan, M. I. Nawaz, and J. Iqbal, "Towards autonomous cleaning of photovoltaic modules: Design and realization of a robotic cleaner," in *Proc. 1st Int. Conf. Latest Trends Electr. Eng. Comput. Technol. (INTELLECT)*, Nov. 2017, pp. 1–6.

[11] M. A. Jaradat, M. Tauseef, Y. Altaf, R. Saab, H. Adel, N. Yousuf, and Y. H. Zurigat, "A fully portable robot system for cleaning solar panels," in *Proc. 10th Int. Symp. Mechatronics Appl. (ISMA)*, Dec. 2015, pp. 1–6.

[12] I. Abuzayed, A. R. Itani, A. Ahmed, M. Alkharaz, M. A. Jaradat, and L. Romdhane, "Design of lightweight aerial manipulator with a CoG compensation mechanism," in *Proc. Adv. Sci. Eng. Technol. Int. Conf. (ASET)*, Feb. 2020, pp. 1–5.

[13] O. M. A. Hafez, M. A. Jaradat, and K. S. Hatamleh, "Stable under-actuated manipulator design for mobile manipulating unmanned aerial vehicle (MM-UAV)," in *Proc. 7th Int. Conf. Modeling, Simulation, Appl. Optim. (ICMSAO)*, Apr. 2017, pp. 1–6.

[14] P. Debenest, M. Guarnieri, K. Takita, E. F. Fukushima, S. Hirose, K. Tamura, A. Kimura, H. Kubokawa, N. Iwama, and F. Shiga, "Sensor-arm—Robotic manipulator for preventive maintenance and inspection of high-voltage transmission lines," in *Proc. IEEE/RSJ Int. Conf. Intell. Robots Syst.*, Sep. 2008, pp. 1737–1744.

[15] L. F. Luque-Vega, B. Castillo-Toledo, A. Loukianov, and L. E. Gonzalez-Jimenez, "Power line inspection via an unmanned aerial system based on the quadrotor helicopter," in *Proc. 17th IEEE Medit. Electrotech. Conf. (MELECON)*, Apr. 2014, pp. 393–397.

[16] A. E. Jimenez-Cano, J. Braga, G. Heredia, and A. Ollero, "Aerial manipulator for structure inspection by contact from the underside," in *Proc. IEEE/RSJ Int. Conf. Intell. Robots Syst. (IROS)*, Sep. 2015, pp. 1879–1884.

[17] M. Fumagalli, R. Naldi, A. Macchelli, R. Carloni, S. Stramigioli, and L. Marconi, "Modeling and control of a flying robot for contact inspection," in *Proc. IEEE/RSJ Int. Conf. Intell. Robots Syst.*, Oct. 2012, pp. 3532–3537.

[18] K. Alexis, G. Darivianakis, M. Burri, and R. Siegwart, "Aerial robotic contact-based inspection: Planning and control," *Auton. Robots*, vol. 40, no. 4, pp. 631–655, Apr. 2016.

[19] A. Ollero, G. Heredia, A. Franchi, G. Antonelli, K. Kondak, A. Sanfeliu, A. Viguria, J. R. Martinez-de Dios, F. Pierri, J. Cortes, A. Santamaria-Navarro, M. A. Trujillo Soto, R. Balachandran, J. Andrade-Cetto, and A. Rodriguez, "The AEROARMS project: Aerial robots with advanced manipulation capabilities for inspection and maintenance," *IEEE Robot. Autom. Mag.*, vol. 25, no. 4, pp. 12–23, Dec. 2018.

[20] Y. Sun, A. Plowcha, M. Nail, S. Elbaum, B. Terry, and C. Detweiler, "Unmanned aerial Auger for underground sensor installation," in *Proc. IEEE/RSJ Int. Conf. Intell. Robots Syst. (IROS)*, Oct. 2018, pp. 1374–1381.

[21] F. Augugliaro, S. Lupashin, M. Hamer, C. Male, M. Hehn, M. W. Mueller, J. S. Willmann, F. Gramazio, M. Kohler, and R. D'Andrea, "The flight assembled architecture installation: Cooperative construction with flying machines," *IEEE Control Syst. Mag.*, vol. 34, no. 4, pp. 46–64, Aug. 2014.

[22] Q. Lindsey, D. Mellinger, and V. Kumar, "Construction of cubic structures with quadrotor teams," in *Robotics: Science and Systems VII*, H. Durrant-Whyte, N. Roy, and P. Abbeel, Eds. Cambridge, MA, USA: MIT Press, 2012, pp. 177–184.

[23] M. Car, A. Ivanovic, M. Orsag, and S. Bogdan, "Impedance based force control for aerial robot peg-in-hole insertion tasks," in *Proc. IEEE/RSJ Int. Conf. Intell. Robots Syst. (IROS)*, Oct. 2018, pp. 6734–6739.

[24] M. Orsag, C. Korpela, S. Bogdan, and P. Oh, "Valve turning using a dual-arm aerial manipulator," in *Proc. Int. Conf. Unmanned Aircr. Syst. (ICUAS)*, May 2014, pp. 836–841, doi: 10.1109/ICUAS.2014.6842330.

[25] P. E. I. Pounds, D. R. Bersak, and A. M. Dollar, "Practical aerial grasping of unstructured objects," in *Proc. IEEE Conf. Technol. Practical Robot Appl.*, Apr. 2011, pp. 99–104, doi: 10.1109/TEPRA.2011.5753489.

[26] H. Seo, S. Kim, and H. J. Kim, "Aerial grasping of cylindrical object using visual servoing based on stochastic model predictive control," in *Proc. IEEE Int. Conf. Robot. Autom. (ICRA)*, May 2017, pp. 6362–6368, doi: 10.1109/ICRA.2017.7989751.

[27] G. Zhang, Y. He, B. Dai, F. Gu, L. Yang, J. Han, G. Liu, and J. Qi, "Grasp a moving target from the air: System & control of an aerial manipulator," in *Proc. IEEE Int. Conf. Robot. Autom. (ICRA)*, May 2018, pp. 1681–1687, doi: 10.1109/ICRA.2018.8461103.

[28] R. Spica, A. Franchi, G. Oriolo, H. H. Bulthoff, and P. R. Giordano, "Aerial grasping of a moving target with a quadrotor UAV," in *Proc. IEEE/RSJ Int. Conf. Intell. Robots Syst.*, Oct. 2012, pp. 4985–4992, doi: 10.1109/IROS.2012.6385771.

[29] J. Ore, S. Elbaum, A. Burgin, and C. Detweiler, "Autonomous aerial water sampling," *J. Field Robot.*, vol. 32, no. 8, pp. 1095–1113, Dec. 2015.

[30] J. R. Kutia, K. A. Stol, and W. Xu, "Canopy sampling using an aerial manipulator: A preliminary study," in *Proc. Int. Conf. Unmanned Aircr. Syst. (ICUAS)*, Jun. 2015, pp. 477–484, doi: 10.1109/ICUAS.2015.7152326.

[31] J. L. J. Scholten, M. Fumagalli, S. Stramigioli, and R. Carloni, "Interaction control of an UAV endowed with a manipulator," in *Proc. IEEE Int. Conf. Robot. Autom.*, May 2013, pp. 4910–4915, doi: 10.1109/ICRA.2013.6631278.

[32] A. Q. L. Keemink, M. Fumagalli, S. Stramigioli, and R. Carloni, "Mechanical design of a manipulation system for unmanned aerial vehicles," in *Proc. IEEE Int. Conf. Robot. Autom.*, May 2012, pp. 3147–3152, doi: 10.1109/ICRA.2012.6224749.

[33] M. Fumagalli, R. Naldi, A. Macchelli, F. Forte, A. Q. L. Keemink, S. Stramigioli, R. Carloni, and L. Marconi, "Developing an aerial manipulator prototype: Physical interaction with the environment," *IEEE Robot. Autom. Mag.*, vol. 21, no. 3, pp. 41–50, Sep. 2014, doi: 10.1109/MRA.2013.2287454.

[34] M. Fumagalli, S. Stramigioli, and R. Carloni, "Mechatronic design of a robotic manipulator for unmanned aerial vehicles," in *Proc. IEEE/RSJ Int. Conf. Intell. Robots Syst. (IROS)*, Oct. 2016, pp. 4843–4848.

[35] M. Kamel, K. Alexis, and R. Siegwart, "Design and modeling of dexterous aerial manipulator," in *Proc. IEEE/RSJ Int. Conf. Intell. Robots Syst. (IROS)*, Oct. 2016, pp. 4870–4876, doi: 10.1109/IROS.2016.7759715.

[36] S. Kim, S. Choi, and H. J. Kim, "Aerial manipulation using a quadrotor with a two DOF robotic arm," in *Proc. IEEE/RSJ Int. Conf. Intell. Robots Syst.*, Nov. 2013, pp. 4990–4995, doi: 10.1109/IROS.2013.6697077.

[37] M. Fanni and A. Khalifa, "A new 6-DOF quadrotor manipulation system: Design, kinematics, dynamics, and control," *IEEE/ASME Trans. Mechatronics*, vol. 22, no. 3, pp. 1315–1326, Jun. 2017, doi: 10.1109/TMECH.2017.2681179.

[38] R. Cano, C. Perez, F. Pruaño, A. Ollero, and G. Heredia, "Mechanical design of a 6-DOF derial manipulator for assembling bar structures using UAVs," Centre Adv. Aerosp. Technol., Univ. Seville, Seville, Spain, Tech. Rep., 2014.

[39] A. Suarez, A. E. Jimenez-Cano, V. M. Vega, G. Heredia, A. Rodriguez-Castaño, and A. Ollero, "Design of a lightweight dual arm system for aerial manipulation," *Mechatronics*, vol. 50, pp. 30–44, Apr. 2018.

[40] A. Suarez, P. R. Soria, G. Heredia, B. C. Arrue, and A. Ollero, "Anthropomorphic, compliant and lightweight dual arm system for aerial manipulation," in *Proc. IEEE/RSJ Int. Conf. Intell. Robots Syst. (IROS)*, Sep. 2017, pp. 992–997, doi: 10.1109/IROS.2017.8202266.

[41] P. E. I. Pounds, D. R. Bersak, and A. M. Dollar, "Stability of small-scale UAV helicopters and quadrotors with added payload mass under PID control," *Auton. Robots*, vol. 33, nos. 1–2, pp. 129–142, Aug. 2012.

[42] G. Antonelli, E. Cataldi, P. R. Giordano, S. Chiaverini, and A. Franchi, "Experimental validation of a new adaptive control scheme for quadrotors MAVs," in *Proc. IEEE/RSJ Int. Conf. Intell. Robots Syst.*, Nov. 2013, pp. 2439–2444, doi: 10.1109/IROS.2013.6696699.

[43] P.-J. Bristeau, P. Martin, E. Salaun, and N. Petit, "The role of propeller aerodynamics in the model of a quadrotor UAV," in *Proc. Eur. Control Conf. (ECC)*, Aug. 2009, pp. 683–688, doi: 10.23919/ECC.2009.7074482.

[44] S. X. Wei, M. R. Burkhardt, and J. Burdick, "Nonlinear controllability assessment of aerial manipulator systems using Lagrangian reduction," *IFAC-PapersOnLine*, vol. 54, no. 19, pp. 100–105, 2021, doi: 10.1016/j.ifacol.2021.11.062.

[45] Y. Ohnishi, T. Takaki, T. Aoyama, and I. Ishii, "Development of a 4-joint 3-DOF robotic arm with anti-reaction force mechanism for a multicopter," in *Proc. IEEE/RSJ Int. Conf. Intell. Robots Syst. (IROS)*, Sep. 2017, pp. 985–991, doi: 10.1109/IROS.2017.8202265.

[46] K. Baizid, G. Giglio, F. Pierri, M. A. Trujillo, G. Antonelli, F. Caccavale, A. Viguria, S. Chiaverini, and A. Ollero, "Behavioral control of unmanned aerial vehicle manipulator systems," *Auton. Robots*, vol. 41, no. 5, pp. 1203–1220, Jun. 2017.

[47] F. Ruggiero, M. A. Trujillo, R. Cano, H. Ascorbe, A. Viguria, C. Perez, V. Lippiello, A. Ollero, and B. Siciliano, "A multilayer control for multirotor UAVs equipped with a servo robot arm," in *Proc. IEEE Int. Conf. Robot. Autom. (ICRA)*, May 2015, pp. 4014–4020, doi: 10.1109/ICRA.2015.7139760.

[48] A. Suarez, M. Perez, G. Heredia, and A. Ollero, "Cartesian aerial manipulator with compliant arm," *Appl. Sci.*, vol. 11, no. 3, p. 1001, 2021, doi: 10.3390/app11031001.

[49] K. Chaisena, K. Chamniprasart, and S. Tantrairatn, "An automatic stabilizing system for balancing a multi-rotor subject to variations in center of gravity and mass," in *Proc. 3rd Int. Conf. Eng. Sci. Innov. Technol. (ESIT)*, Apr. 2018, pp. 1–5.

[50] G. Garofalo, F. Beck, and C. Ott, "Task-space tracking control for underactuated aerial manipulators," in *Proc. Eur. Control Conf. (ECC)*, Jun. 2018, pp. 628–634, doi: 10.23919/ECC.2018.8550248.

[51] A. Y. Mersha, S. Stramigioli, and R. Carloni, "Exploiting the dynamics of a robotic manipulator for control of UAVs," in *Proc. IEEE Int. Conf. Robot. Autom. (ICRA)*, May 2014, pp. 1741–1746, doi: 10.1109/ICRA.2014.6907086.

[52] E. Fresk, D. Wuthier, and G. Nikolakopoulos, "Generalized center of gravity compensation for multirotors with application to aerial manipulation," in *Proc. IEEE/RSJ Int. Conf. Intell. Robots Syst. (IROS)*, Sep. 2017, pp. 4424–4429, doi: 10.1109/IROS.2017.8206307.

[53] V. Sumathy, S. A. M. Abdul, and D. Ghose, "Projection operator-based robust adaptive control of an aerial robot with a manipulator," *J. Field Robot.*, vol. 40, no. 5, pp. 1–28, 2023, doi: 10.1002/rob.22168.

[54] I. Palunko and R. Fierro, "Adaptive control of a quadrotor with dynamic changes in the center of gravity," *IFAC Proc. Volumes*, vol. 44, no. 1, pp. 2626–2631, Jan. 2011.

[55] M. Orsag, C. Korpela, S. Bogdan, and P. Oh, "Lyapunov based model reference adaptive control for aerial manipulation," in *Proc. Int. Conf. Unmanned Aircr. Syst. (ICUAS)*, May 2013, pp. 966–973, doi: 10.1109/ICUAS.2013.6564783.

[56] S. Kannan, M. Alma, M. A. Olivares-Mendez, and H. Voos, "Adaptive control of aerial manipulation vehicle," in *Proc. IEEE Int. Conf. Control Syst., Comput. Eng. (ICCSCE)*, Nov. 2014, pp. 273–278, doi: 10.1109/ICCSCE.2014.7072729.

[57] Y. Chen, W. Zhan, B. He, L. Lin, Z. Miao, X. Yuan, and Y. Wang, "Robust control for unmanned aerial manipulator under disturbances," *IEEE Access*, vol. 8, pp. 129869–129877, 2020, doi: 10.1109/ACCESS.2020.3008971.

[58] S. Briot, V. Arakelian, and J.-P. Le Baron, "Shaking force minimization of high-speed robots via centre of mass acceleration control," *Mechanism Mach. Theory*, vol. 57, pp. 1–12, Nov. 2012.

[59] Y. Vyas, A. Pasetto, V. Ayala-Alfaro, N. Massella, and S. Cocuzza, "Null-space minimization of center of gravity displacementof a redundant aerial manipulator," *Robotics*, vol. 12, no. 2, p. 31, Feb. 2023, doi: 10.3390/robotics12020031.

[60] Y. S. Sarkisov, A. Coelho, M. G. Santos, M. J. Kim, D. Tsetserukou, C. Ott, and K. Kondak, "Hierarchical whole-body control of the cable-suspended aerial manipulator endowed with winch-based actuation," in *Proc. IEEE Int. Conf. Robot. Autom. (ICRA)*, May 2023, pp. 5366–5372.

[61] A. G. Gray, F. Gonzalez, F. Vanegas, J. Galvez-Serna, and K. Morton, "Design and flight testing of a UAV with a robotic arm," in *Proc. IEEE Aerosp. Conf.*, Big Sky, MT, USA, Mar. 2023, pp. 1–13, doi: 10.1109/AERO55745.2023.10115880.

[62] K. Bouzgou, L. Benchikh, L. Nouveliere, Z. Ahmed-Foitih, and Y. Bestaoui, "Combined algorithms for analytical inverse kinematics solving and control of the Q-PRR aerial manipulator," *Mech. Based Des. Struct. Mach.*, pp. 1–23, 2022, doi: 10.1080/15397734.2022.2151467.

[63] DJI Official. (2021). *Flame Wheel ARF KIT—DJI*. [Online]. Available: https://www.dji.com/ae/flame-wheel-arf

[64] S. Lessard, P. Bigras, and I. A. Bonev, "A new medical parallel robot and its static balancing optimization," *J. Med. Devices*, vol. 1, no. 4, pp. 272–278, Dec. 2007.

[65] *Fusion 360*, Autodesk, San Francisco, CA, USA, 2020.

[66] L. Zhao, A. K. W. Yen, J. Coulombe, P. Bigras, and I. A. Bonev, "Kinematic analyses of a new medical robot for 3D vascular ultrasound examination," *Trans. Can. Soc. Mech. Eng.*, vol. 38, no. 2, pp. 227–239, Jun. 2014, doi: 10.1139/tcsme-2014-0016.

[67] L. Zhao, A. Joubair, P. Bigras, and I. A. Bonev, "Metrological evaluation of a novel medical robot and its kinematic calibration," *Int. J. Adv. Robot. Syst.*, vol. 12, no. 9, p. 126, Sep. 2015, doi: 10.5772/60881.

[68] D. Ilia and R. Sinatra, "A novel formulation of the dynamic balancing of five-bar linkages with applications to link optimization," *Multibody Syst. Dyn.*, vol. 21, no. 2, pp. 193–211, Mar. 2009, doi: 10.1007/s11044-008-9134-2.

[69] V. Lippiello and F. Ruggiero, "Cartesian impedance control of a UAV with a robotic arm," *IFAC Proc. Volumes*, vol. 45, no. 22, pp. 704–709, 2012.

[70] F. Caccavale, G. Giglio, G. Muscio, and F. Pierri, "Adaptive control for UAVs equipped with a robotic arm," *IFAC Proc. Volumes*, vol. 47, no. 3, pp. 11049–11054, 2014.

[71] B. Siciliano, L. Sciavicco, L. Villani, and G. Oriolo, *Robotics: Modeling, Planning and Control*. New York, NY, USA: Springer, 2010.

[72] S. Kannan, M. A. Olivares-Mendez, and H. Voos, "Modeling and control of aerial manipulation vehicle with visual sensor," *IFAC Proc. Volumes*, vol. 46, no. 30, pp. 303–309, 2013.

[73] M. W. Spong, S. A. Hutchinson, and M. Vidyasagar, "Robot modeling and control," *IEEE Control Syst.*, vol. 26, no. 6, pp. 113–115, Dec. 2006.

[74] K. Sollmann and M. Jouaneh, "Dynamic modelling of a single-axis belt-drive system," *Int. J. Model., Identificat. Control*, vol. 12, no. 4, p. 386, 2011, doi: 10.1504/IJMIC.2011.040082.

[75] G. Zhang, Y. He, B. Dai, F. Gu, J. Han, and G. Liu, "Robust control of an aerial manipulator based on a variable inertia parameters model," *IEEE Trans. Ind. Electron.*, vol. 67, no. 11, pp. 9515–9525, Nov. 2020, doi: 10.1109/TIE.2019.2956414.

[76] C. M. Close and D. K. Frederick, *Modeling and Analysis of Dynamic Systems*. Boston, MA, USA: Houghton Mifflin, 1993.

[77] A. Isidori, *Nonlinear Control Systems*. London, U.K.: Springer, 1995.

MUHANNAD ALKADDOUR (Member, IEEE) received the B.Sc. degree in mechanical engineering and mathematics from the American University of Sharjah (AUS), in 2018, and the M.Sc. degree from the Mechatronics Engineering Graduate Program, AUS, in 2020. He is currently pursuing the Ph.D. degree in mechanical engineering with the University of Michigan, Ann Arbor. His current research interests and research experience are in dynamics and control systems, robotics, mechanical vibrations, and deep learning.

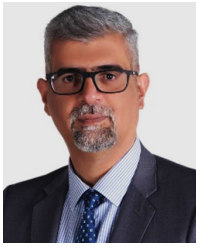

MOHAMMAD A. JARADAT received the master's and Ph.D. degrees in mechanical engineering from Texas A&M University, College Station, TX, USA. He is currently with the American University of Sharjah (AUS) and the Mechanical Engineering Department, Jordan University of Science and Technology (JUST). He is also a part of the Mechatronics Graduate Program, AUS. His scientific experience has resulted in many publications, patents, projects, and awards specialized in the following research areas: robotics, artificial intelligent systems, sensor fusion, fault diagnostics, intelligent NANO-systems, intelligent control, mechatronics system design, and control systems.

SARA TELLAB received the B.Sc. degree (summa cum laude) in electrical engineering/communications from Ajman University, United Arab Emirates, in 2017, and the M.Sc. degree in mechatronics engineering from the American University of Sharjah (AUS), in 2020. She joined the Mechatronics Graduate Program at AUS in 2018, where she was a Graduate Teaching Assistant. Her current research interests include machine learning, image processing, computer vision, and mobile robots.

NIDAL A. SHERIF received the B.S. degree in mechanical engineering from the American University of Sharjah, Sharjah, United Arab Emirates, in 2019. Has has since gone on to pursue a career in robotics engineering, where he is currently working on greenhouse automation. His research interests include autonomous systems, autonomous navigation and localization, state estimation, and control systems. In 2022, he was awarded the M.S. degree in Mechatronics Engineering by the American University of Sharjah.

MUHAMMAD H. ALVI received the B.S. degree in mechanical engineering from the American University of Sharjah, Sharjah, United Arab Emirates (UAE), in 2020. He is currently pursuing the M.S. degree in engineering technology with Purdue University, USA. His work experience consists of two years of full-time employment with AstraUTM, Dubai, UAE. He worked with various UAV systems and designed, built, and test complex payloads. He was an Undergraduate Research Assistant with the American University of Sharjah, where he worked on designing aerial manipulator systems and com-pliant airfoil designs. His current research interests include mechatronics systems, robotics, kinematic and dynamic modelling, and mechanical design.

LOTFI ROMDHANE (Member, IEEE) received the Ph.D. degree in mechanical engineering from the University of Florida, USA. He held academic positions with King Saud University, Saudi Arabia; and the University of Monastir and the University of Sousse, Tunisia. He was a Visiting Professor in France and Poland. He is currently a Professor/an Associate Dean of the Graduate Affairs and Research, College of Engineering. His research interests include robotics, mechanisms, machine design, biomechanics of motion, and mechatronics. He has taught several undergraduate and graduate courses in these fields and supervised over 15 Ph.D. students and 30 master's students. He is a member of the Technical Committee for Computational Kinematics and the Robotics and Mechatronics of the International Federation for the Promotion of Mechanisms and Machines (IFToMM).

KHALED S. HATAMLEH received the B.Sc. degree in mechanical engineering from the Jordan University of Science and Technology (JUST), Jordan, in 2002, the M.Sc. degree in industrial automation engineering from Yarmouk University, Jordan, in 2006, and the Ph.D. degree in mechanical engineering from New Mexico State University, Las Cruces, NM, USA, in 2010. He is currently an Associate Professor with the Mechanical Engineering Department, JUST. His research interests include robotics, UAV parameter estimation, IMU, and control systems.